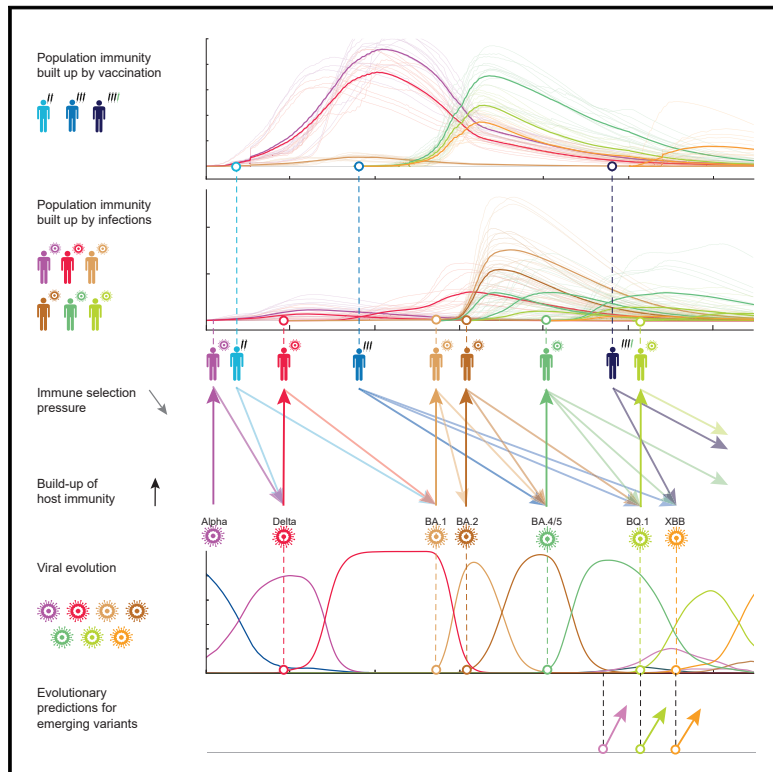


Population immunity predicts evolutionary trajectories of SARS-CoV-2

Graphical abstract



Authors

Matthijs Meijers, Denis Ruchnewitz,
Jan Eberhardt, Marta Łuksza,
Michael Lässig

Correspondence

mlaessig@uni-koeln.de

In brief

A cross-scale analysis of acquired population immunity maps evolutionary forces of SARS-CoV-2 and predicts near-future changes of viral variants based on molecular data and time-resolved surveillance.

Highlights

- SARS-CoV-2 variants compete on a fitness landscape shaped by population immunity
- Immune-induced fitness is computable from **genetic, epidemic, and cross-protection data**
- A fitness model predicts **viral frequency changes and predominance shifts**
- Time-dependent selection windows constrain the antigenic profile of emerging variants

Article

Population immunity predicts evolutionary trajectories of SARS-CoV-2

Matthijs Meijers,¹ Denis Ruchnewitz,¹ Jan Eberhardt,¹ Marta Łuksza,² and Michael Lässig^{1,3,*}

¹Institute for Biological Physics, University of Cologne, Zülpicherstr. 77, 50937 Köln, Germany

²Tisch Cancer Institute, Departments of Oncological Sciences and Genetics and Genomic Sciences, Icahn School of Medicine at Mount Sinai, New York, NY, USA

³Lead contact

*Correspondence: mlaessig@uni-koeln.de

<https://doi.org/10.1016/j.cell.2023.09.022>

SUMMARY

The large-scale evolution of the SARS-CoV-2 virus has been marked by rapid turnover of genetic clades. New variants show intrinsic changes, notably increased transmissibility, and antigenic changes that reduce cross-immunity induced by previous infections or vaccinations. How this functional variation shapes global evolution has remained unclear. Here, we establish a predictive fitness model for SARS-CoV-2 that integrates antigenic and intrinsic selection. The model is informed by tracking of time-resolved sequence data, epidemiological records, and cross-neutralization data of viral variants. Our inference shows that immune pressure, including contributions of vaccinations and previous infections, has become the dominant force driving the recent evolution of SARS-CoV-2. The fitness model can serve continued surveillance in two ways. First, it successfully predicts the short-term evolution of circulating strains and flags emerging variants likely to displace the previously predominant variant. Second, it predicts likely antigenic profiles of successful escape variants prior to their emergence.

INTRODUCTION

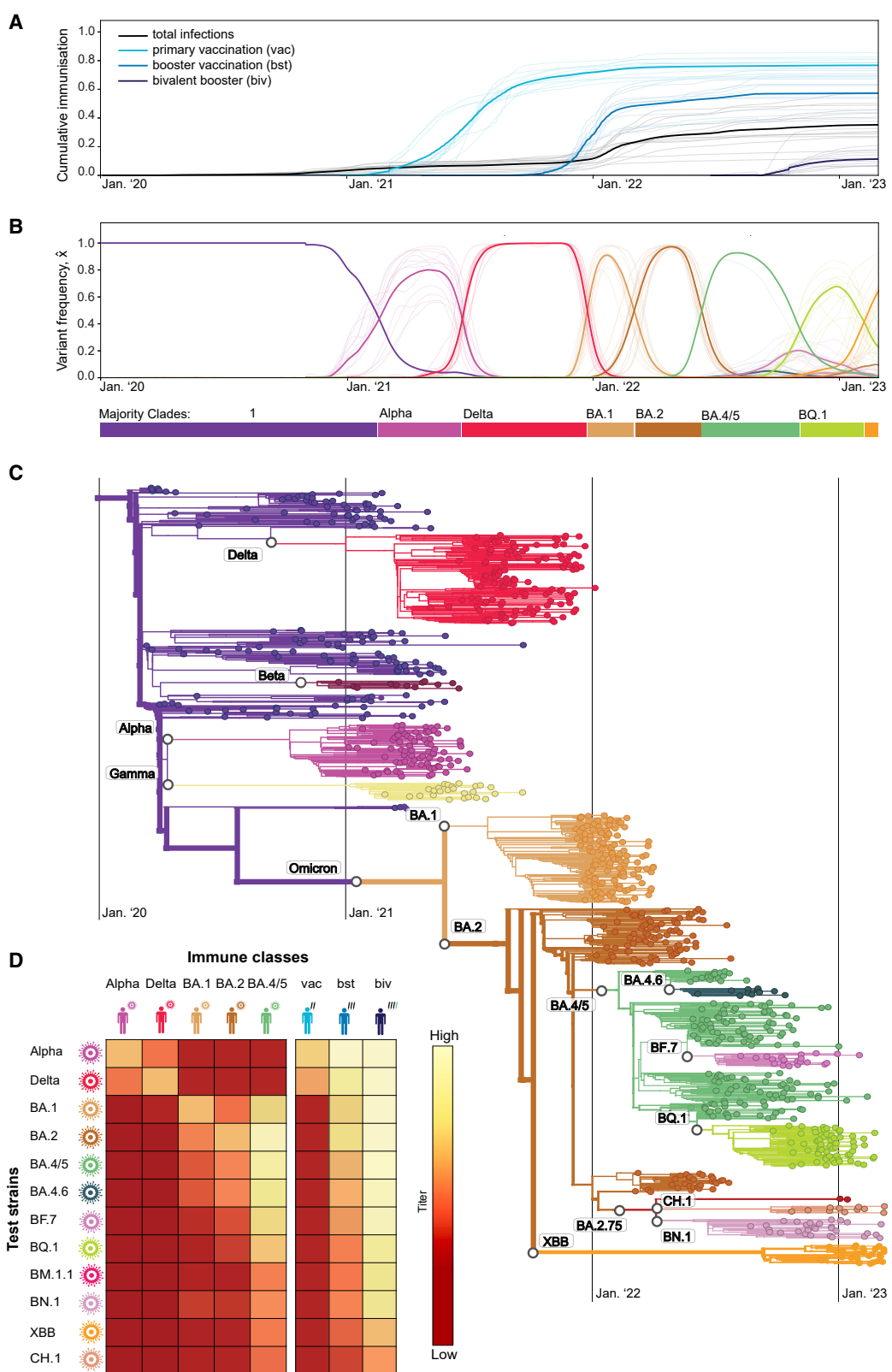
Two classes of molecular adaptation have been observed in the evolution of SARS-CoV-2 to date. Multiple mutations carry intrinsic changes of viral functions, such as increasing the binding affinity to human receptors,¹ the efficiency of cell entry,^{2,3} or the stability of viral proteins.^{4,5} Other mutations, referred to as antigenic changes, decrease the neutralizing activity of human antibodies,^{6–10} thereby reducing the immune protection against secondary infections.^{11,12} The strains descending from a given mutant strain define a clade of the evolving viral population. Several of these molecular changes had drastic evolutionary and epidemiological impact, inducing global turnover of viral clades and concurrent waves of the pandemic. Since the start of the pandemic, 7 major evolved variants successively gained global predominance: Alpha and Delta in 2021, and the Omicron variants BA.1, BA.2, BA.4/5, BQ.1, and XBB since 2022. These were named Variants of Concern (VOCs) by the World Health Organization¹³; other VOCs gained temporary regional majority. Several studies reported fitness advantages of VOCs inferred from epidemiological trajectories and comparative functional studies.^{3,14–17} Importantly, however, the evolutionary impact of antigenic changes is time-dependent because it depends on previously acquired population immunity: a larger amount of previous infections or vaccinations increases the global fitness advantage of an antigenic escape mutation. Specifically, multi-strain epidemiological models and simulations suggest that

vaccinations can favor the emergence of escape variants^{18–21} and influence the turnover of circulating clades^{22,23}; effects of this kind have been reported for some clades of human influenza.²⁴ In the case of SARS-CoV-2, pandemic infection and massive vaccination programs, with a global count of >10 billion vaccinations and >700 million confirmed cases up to March 1, 2023,²⁵ have built up partial population immunity, but its feedback on viral evolution has not been quantified. This leads to the central questions of this paper: what is the feedback of vaccination and infection on the subsequent turnover of SARS-CoV-2 clades, and how can this information be harvested for evolutionary predictions? To address these questions, we infer a data-driven fitness model for SARS-CoV-2 variants with distinct components of intrinsic fitness and antigenic fitness induced by vaccination and infection.

RESULTS

Evolutionary, epidemiological, and immune tracking of SARS-CoV-2

As a basis for our fitness model, we track time-resolved data of SARS-CoV-2 in a set of 13 regions (countries or US states) that satisfy uniform criteria of data availability for the period of main interest for this study (spring 2021 to present; these criteria are detailed in [STAR Methods](#)). First, we obtain the cumulative population fractions of reported infections and of primary, booster, and bivalent-booster vaccinations.^{25,26} These data show that



(legend on next page)

population immunity rose sharply during the SARS-CoV-2 pandemic, first primarily by vaccination, and later also by more frequent infections (Figure 1A).

Second, we track the evolution of SARS-CoV-2 from a set of >8 million quality-controlled SARS-CoV-2 sequences obtained from the GISAID database.²⁷ Sequences are assigned to genetic clades using a standard set of amino acid changes²⁸; time-dependent clade frequencies, $\hat{x}_i(t)$ ($i = 1$, Alpha, Delta, ...), are inferred from strain counts smoothed over a period of 30 days in each region (Figure 1B). Here, 1 denotes the set of clades circulating prior to Alpha, including the wild type (wt) and the early 614G mutation in the spike protein. A sequence-based timed tree shows the genealogical relationships between these clades (Figure 1C; see STAR Methods for details of tree reconstruction). The evolutionary tracking of SARS-CoV-2 displays the well-known clade shifts to successive major variants, 1–Alpha, Alpha–Delta, Delta–BA.1, BA.1–BA.2, BA.2–BA.4/5, BA.4/5–BQ.1, and BQ.1–XBB. The variants BA.4 and BA.5 are treated as a single clade because they have identical spike proteins. Starting in 2022, we note an increased diversity, with multiple sub-clades of BA.2 and BA.4/5 circulating simultaneously at significant frequency.

Third, we record the antigenic evolution of SARS-CoV-2 from molecular cross-immunity data between variants. Cross-immunity induced by a primary infection against subsequent infections by related pathogens is routinely tested by neutralization assays, which measure the minimum antiserum concentration required to neutralize the second antigen. Relative inverse concentrations are reported as serum dilution titers; here we use logarithmic titer values, T (with base 2). For SARS-CoV-2, recent work^{7–9,29–32} has established a matrix of titers, T_i^k , measuring neutralization of variant i in immunization class k (Table S1). These immunization classes distinguish infections by different variants ($k = \text{Alpha, Delta, BA.1, ...}$), as well as primary, booster, and bivalent booster vaccinations ($k = \text{vac, bst, biv}$). Together, these data provide a coarse-grained cross-immunity landscape of SARS-CoV-2 (Figure 1D). Infection-induced cross-immunity titers are maximal when primary infection and secondary challenge are by the same variant; antigenic evolution generates a gradual decline in subsequent variants. Cross-immunity induced by wt-based vaccines declines in a similar way for primary vaccination, mostly in the clade shifts from Alpha to BA.1 and for wt boosters in the shifts from BA.1 to XBB. For bivalent boosters, significant titer drops are first observed in the currently most advanced variants, XBB and CH.1.

Population immunity trajectories

Recent work for SARS-CoV-2 has shown that neutralization titers predict the cross-immunity c_i^k , defined as the relative drop

of secondary infections in human cohorts. This dependence is approximately given by a Hill function,^{11,12} $c_i^k = H(T_i^k)$, for secondary infections shortly after the primary immunization. This form is consistent with the underlying biophysics of antibody-antigen binding and with results for other viral pathogens.^{33–36} The intra-host concentration of neutralizing antibodies decays exponentially with time after immunization.^{37,38} This translates into a linear titer reduction, such that the cross-immunity at later times is given as $c_i^k(\Delta t) = H(T_i^k - \Delta t/\tau)$. Together, cross-immunity depends in a predictable, nonlinear way on neutralization titer and on time since primary immunization.

To track population immunity over time, we combine the cross-immunity factors $c_i^k(\Delta t)$ with the population rates of new infections and vaccinations, $\omega_k(t)$, in different immunization classes, k . Here, clade-specific infection data are obtained by multiplying the total rate of new infections reported in each region, $\omega_{\text{inf}}(t)$ (i.e., the time derivative of the cumulative population fraction shown in Figure 1A), with the simultaneous viral clade frequencies, $\omega_k(t) = \hat{x}_k(t) \omega_{\text{inf}}(t)$ (Figure 1B). Together, we infer the population cross-immunity against clade i by immunization in class k ,

$$C_i^k(t) = \int_0^t c_i^k(t-t') \omega_k(t') dt'. \quad (\text{Equation 1})$$

Figure 2 shows the resulting regional and region-averaged population immunity trajectories for multiple immune classes and viral variants. These trajectories integrate three factors of change: increase by recent infections or vaccinations, decrease by intra-host antibody decay, and viral escape evolution.

Fitness model

To quantify the feedback of cross-immunity on viral evolution, we use a minimal computable fitness model,

$$F_i(t) = F_i^0 - \sum_k \gamma_k C_i^k(t), \quad (\text{Equation 2})$$

where $F_i(t)$ is the absolute fitness, or epidemic growth rate, of a viral variant. We compute fitness at the level of variants, neglecting fitness differences between strains within a clade. Absolute fitness depends on the effective reproductive number (the average number of new infections generated by an infected individual) and on the distribution of generational intervals (the time between infection and transmission)^{39,40} (STAR Methods). Here, we write fitness as the sum of a time-independent intrinsic component, F_i^0 , and of time-dependent antigenic components, $F_i^k(t) = -\gamma_k C_i^k(t)$ (STAR Methods). Each component is proportional to the corresponding cross-immunity factor $C_i^k(t)$ with a

Figure 1. Evolutionary, epidemiological, and immune tracking of SARS-CoV-2

- (A) Cumulative population fractions of infections and of primary, booster, and bivalent booster vaccinations; data from all longitudinally tracked regions of this study (thin lines) and region-averaged trajectories (thick lines). A list of regions and selection criteria are given in STAR Methods.
- (B) Frequency trajectories for the ancestral clade (1), 7 major variant clades (Alpha, Delta, BA.1, BA.2, BA.4/5, BQ.1, and XBB), and 5 global minor variant clades (BA.4.6, BA.7, BM.1.1, BN.1, and CH.1). Regional data are shown by thin lines; region-averaged trajectories are shown by thick lines. Color bars mark the succession of major variants.
- (C) Timed global strain tree of SARS-CoV-2 with strains colored by variant. Variants are annotated at the inferred time of their emergence.
- (D) Neutralization titers, T_i^k , for test strains of different variants ($i = \text{Alpha, ..., CH.1}$) assayed in different immune classes of infection ($k = \text{Alpha, ..., BA.4/5}$) and vaccination ($k = \text{vac, bst, biv}$). Numerical values are given in Table S1; the inference procedure is described in STAR Methods.

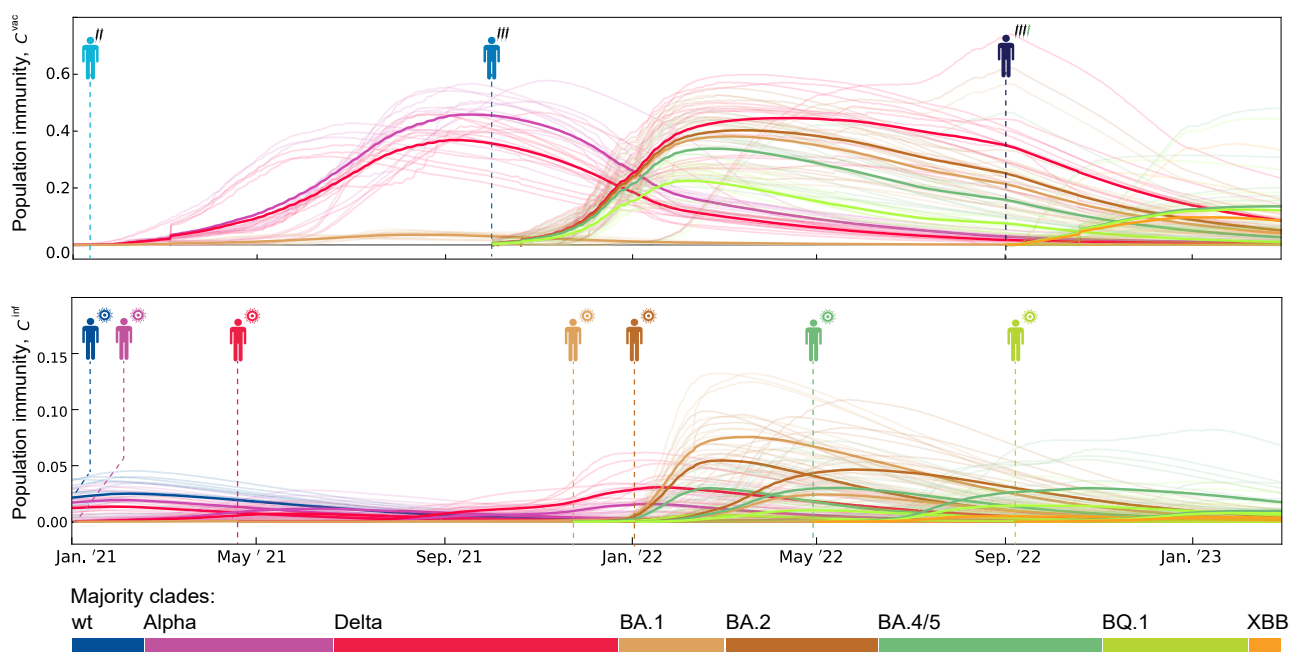


Figure 2. Population immunity trajectories

The time-dependent population immunity, $C_i^k(t)$, is shown for the major variants, i (colored lines), and the immune classes, k (indicated by pictograms), relevant for this study. Trajectories for each immune class start at the dashed line (top, vaccination-derived immune classes, $k = \text{vac}, \text{bst}, \text{biv}$; bottom, infection-derived immune classes, $k = \text{Alpha}, \text{Delta}, \dots, \text{BQ.1}$). Thin lines show region-specific trajectories; thick lines show region-averaged trajectories.

weight factor γ_k for each immune class k . Hence, antigenic selection is generated by cross-immunity differences between competing strains. The relative fitness, or growth rate difference to the mean population, of a given variant governs its adaptive frequency change, as predicted by the fitness model,

$$\frac{d}{dt}x_i(t) = x_i(t) f_i(t), \quad (\text{Equation 3})$$

where $f_i(t) = F_i(t) - \sum_j x_j(t)F_j(t)$. This type of fitness model has been established for evolutionary predictions of human influenza^{22,41,42} and is grounded in multi-strain epidemiological models.^{43–45} Here we develop model-based predictions based on human cross-immunity data, systematically including vaccination effects. In this model, Equations 1, 2, and 3 describe the co-evolution of the viral population and human population immunity. The minimal fitness model does not account for differences in cross-immunity between human hosts in the same immune class (for example, through differences in immunodominance⁴⁶) and for correlations between multiple prior infections (antigenic sin⁴⁷).

Model training and validation

To calibrate the fitness model, we use empirical fitness values inferred from observed frequency trajectories. Assuming that large-scale frequency shifts of viral clades are adaptive processes, we apply the reverse of Equation 3, $\hat{f}_i(t) = (d\hat{x}_i(t)/dt)/\hat{x}_i(t)$, to the tracked frequency data (Figure 1B). Empirical frequency and fitness trajectories are distinguished by a hat from their model-based counterparts. We infer the

maximum-likelihood (ML) fitness model by comparing these empirical fitness trajectories with their model-based counterparts, $f_i(t)$, computed from Equations 1 and 2. The model-based fitness values are derived from regional population immunity trajectories for all regions included in the analysis. We use a minimal antigenic model with just two dynamical parameters (**STAR Methods**): a uniform γ_{vac} for vaccination and boosting (downweighted in the shifts Delta–BA.1 and later to account for double infections⁴⁸) and a uniform $\gamma_k = b\gamma_{\text{vac}}$ for all infection classes k (upweighted by a factor b to correct for relative underreporting; this factor is updated from past infection data).

A region- and time-resolved analysis is essential for the accurate inference of selection because it allows the model to delineate spatial and temporal variation of selection. Growth differences between regions reflect inhomogeneous conditions of contact limitations, surveillance, geography, and population structure that are not included in the minimal model. In a given region, however, variants compete under more homogeneous conditions, and growth rate differences, $s_{ij}(t) = f_i(t) - f_j(t)$, reflect selection. Our model calibration procedure focuses on the frequency trajectories of major variants, which allow a reliable evaluation of empirical selection coefficients in all regions of this study (**Data S1**). Because the temporal variation of model selection coefficients, $s_{ij}(t)$, in a given region depends only on antigenic selection, we can separately infer antigenic and intrinsic selection components. Details of the inference procedure are given in **STAR Methods**; ML model parameters and selection coefficients for all clade shifts are reported in **Tables S2** and **S3**.

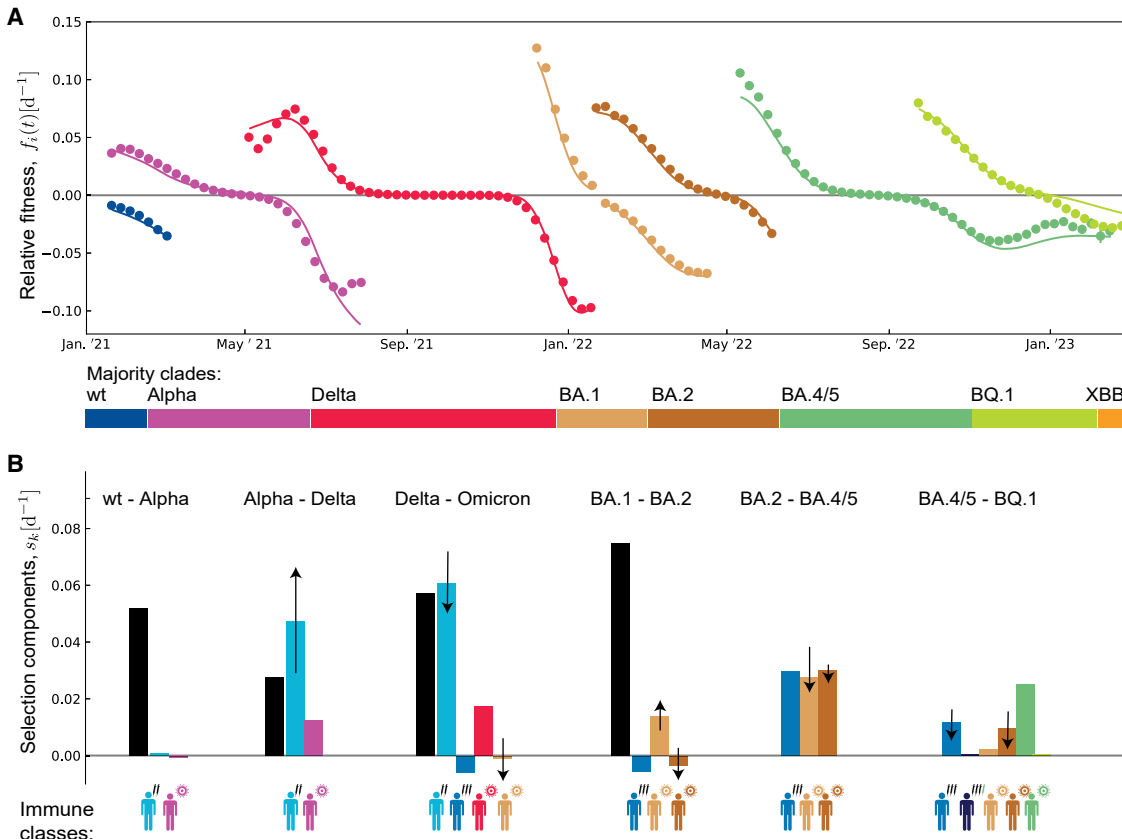


Figure 3. Fitness trajectories and selection breakdown for major clade shifts

(A) Relative fitness of successive major variants in 7 completed clade shifts (1–Alpha, ... BA.4/5–BQ.1). Model-based trajectories for each variant, $f_i(t)$ (lines), are shown in the time interval between origination and loss; empirical fitness values, $\hat{f}_i(t)$ (dots), are inferred from the frequency trajectories of Figure 1B. All trajectories are averaged over 13 regions; see Figure S1 for regional trajectories. Color bars mark the succession of major variants.

(B) Breakdown of selection for each clade shift. Intrinsic selection coefficients, s_0 (black), and antigenic selection coefficients in marked immune classes, s_k (colored), as inferred from the ML fitness model (bars, region- and time-averaged value for each crossover; arrows, region-averaged root mean square (rms) temporal change, $((\Delta s_k)^2)^{1/2}$, with marked direction; confidence intervals are given in Table S3).

In Figure 3A, we plot the resulting ML fitness trajectories, $f_i(t)$, against the corresponding empirical trajectories, $\hat{f}_i(t)$ (dots), for the sequence of major variants 1, Alpha, ..., BQ.1. These trajectories are averaged over all 13 regions; region-specific results are given in Figure S1. We obtain a remarkable data compression: the antigenic fitness computed from Equation 2 reproduces the empirical fitness changes in multiple regions and clade shifts.

The antigenic fitness seascape

Our fitness model posits that time-dependent selection is predominantly antigenic, i.e., caused by differences in population immunity against competing variants. Antigenic selection generates two opposing effects. A high rate of recent infections or vaccinations induces increasing positive selection for an antigenic escape variant by strengthening population immunity against previous variants. Conversely, waning of population immunity against ancestral variants, as well as immunity generated by the invading variant against itself, can decrease antigenic selection over time. Here, we trace both of these effects in the dynamics of clade shifts. From the fitness model, we compute

the time-dependent selection coefficient between ancestral and invading variants, $s(t) = F_{\text{inv}}(t) - F_{\text{anc}}(t)$, and its decomposition into intrinsic and antigenic selection, $s(t) = s_0 + s_{\text{ag}}(t)$ with $s_{\text{ag}}(t) = \sum_k s_k(t)$ (arrows in Figure 3B); this computation uses past epidemic data (Figures 1 and 2). For the Alpha–Delta shift, we find a net increase of selection, caused predominantly by the concurrent buildup of vaccination-induced immunity against Alpha. For the subsequent shifts Delta–BA.1, BA.2–BA.4/5, and BA.4/5–BQ.1, immune waning and self-immunity generate a net decrease of selection. For the early shift 1–Alpha, selection is only weakly time-dependent because ancestral and invading variants are antigenically similar and population immunity is still small; for BA.1–BA.2, selection components of opposite time dependence generate a similarly small net effect. This pattern is confirmed by the empirical selection pattern inferred from regional clade frequency data (Figure S2). During the Alpha–Delta shift, selection increases with time in 16/16 regional trajectories; during the Delta–BA.1, BA.2–BA.4/5, and BA.4/5–BQ.1 shifts, selection decreases in 35/37 trajectories. Hence, compared to a reference of time-independent selection, the

Alpha–Delta shift runs at an accelerating speed, and the three subsequent shifts run at a decelerating speed. In all 4 cases, the temporal variation of selection is statistically significant ($P < 10^{-11}$ for each shift; two-sided Wald test) and substantial (a linear regression gives $\text{Var}(s_{\text{lin}}) > 2 \times 10^{-3} \text{d}^{-2}$). In the remaining shifts, the time dependence of selection is insignificant or weak ($P > 0.01$ for 1–Alpha; $\text{Var}(s_{\text{lin}}) = 3 \times 10^{-4} \text{d}^{-2}$ for BA.1–BA.2).

To test our fitness model and selection inference, we examine whether intrinsic selection can produce a comparable signal of time dependence. Sources of intrinsic selection include changes in transmissibility, intra-host replication rate, and pathogenicity, which affect the basic reproductive number and the distribution of generation intervals. Such changes have been reported for some of the early major variants.^{1,3,49,50} In **STAR Methods**, we show that the resulting intrinsic selection is coupled to absolute growth in some cases (Figure S3). Because absolute growth depends on time through multiple factors, including temperature, population density, and non-pharmaceutical containment measures, this coupling could induce time-dependent intrinsic selection, at variance with our fitness model.⁴⁰ To assess this possibility, we evaluate the empirical variation of absolute growth along regional trajectories. We find only a small co-variation with selection and hence no evidence for time-dependent intrinsic selection (**STAR Methods**; Figure S3). We conclude that antigenic changes are the dominant source of time-dependent selection, corroborating our minimal fitness model and the resulting decomposition of selection (Figure 3B). Similarly, our inference of selection is robust under time-dependent non-pharmaceutical interventions (**STAR Methods**; Figure S3).

Intrinsic, infection-induced, and vaccination-induced selection

The ML fitness model provides a breakdown of the selection forces driving the observed sequence of major clade shifts (Figure 3B). Intrinsic selection is strong and positive in the pre-BA.2 shifts, with average selection coefficients $s_0 = 0.03 - 0.08$ between invading and ancestral variants, consistent with strong functional differences observed between early variants^{3,51} (Table S3, all selection coefficients are given in units d^{-1}). In the post-BA.2 shifts, intrinsic selection is inferred to be small (a recent exception, XBB.1.5, will be noted below). Antigenic selection follows an opposite trend: the average selection coefficients between invading and ancestral variants are initially small but reach values $s_{\text{ag}} \geq 0.05$ in all post-Alpha shifts except BA.1–BA.2. The recent decline, from $s_{\text{ag}} \approx 0.08$ for Delta–BA.1 and BA.2–BA.4/5 to $s_{\text{ag}} = 0.05$ for BA.4/5–BQ.1, reflects decreasing infection and vaccination rates toward the end of the pandemic, as well as waning protection from earlier immunizations. Consistently, the empirical total selection declines from its peak value $\hat{s} = 0.13 \pm 0.03$ for Delta–BA.1 to $\hat{s} = 0.05 \pm 0.01$ for BA.4/5–BQ.1; that is, evolution decelerates in the transition to an endemic state.

Of particular interest is the pattern of vaccination-induced antigenic selection, which maps the feedback of vaccination on the subsequent evolutionary trajectory of the virus (Figure 3B). Primary vaccination contributes substantial positive selection, $s_{\text{vac}} = 0.05 - 0.06$, in the shifts Alpha–Delta and Delta–BA.1, which are the main steps of antigenic escape from the wt-based

vaccine (Figure 1B). Booster vaccinations have increased breadth compared to primary vaccinations^{8,9,52,53} (Table S1; Figure 1D); that is, they induce higher cross-immunity and initially weaker selection for antigenic escape. In the Delta–BA.1 shift, boosters even generate a negative selection coefficient $s_{\text{bst}} = -0.01$ because they remove cross-immunity differences and antigenic selection generated by the preceding primary vaccination. Positive selection is inferred for the post-BA.2 shifts when the virus partially escapes from booster-induced immunity (Figure 1D). Similarly, positive selection induced by bivalent boosters is first seen in the new variants XBB and CH.1 and is expected to peak in the post-BQ.1 shifts (see Figure 5 below).

Vaccination- and infection-induced selection are statistically significant parts of the calibrated fitness model for SARS-CoV-2 (Figure 3B); partial models with only one component have a strongly reduced posterior likelihood (differences in model complexity are accounted for by a Bayesian information criterion; see **STAR Methods** and Table S2). These results show that vaccination and previous infections induced sizable antigenic selection on circulating SARS-CoV-2 variants and modulated the speed of successive clade shifts. However, the fitness model and our data analysis do not predict any simple relation between vaccination coverage and the speed of evolution. This is because cross-immunity classes are correlated: fewer vaccinations lead to more infections, generating a buildup of cross-immunity in other classes and complex long-term effects.

Predicting short-term evolution

The post-BA.2 evolution of SARS-CoV-2 is characterized by the prevalence of antigenic selection (Figure 3B) and by the emergence of multiple competing antigenic variants. Besides the major variants BA.4/5, BQ.1, and XBB, these include the clades BA.4.6, BF.7, BN.1, and CH.1, all of which show initial growth and antigenic differences from their parent clade (Figures 1C and 1D). Can the fitness model predict the short-term evolution of such complex viral populations? To address this question, we first plot the timed tree of all strains descending from BA.2, coloring each isolate by the relative fitness computed from the antigenic fitness components at the time of sampling, $f_i^{\text{ag}}(t)$ (Figure 4A). The fitness model is seen to predict subsequent frequency shifts of clades: high fitness signals frequency increase, and low fitness signals frequency decline.

To assess the predictive power more quantitatively, we compare predicted frequency changes, $W_i(t, t + \tau) = x_i(t + \tau)/\hat{x}_i(t)$, with their observed counterparts, $\hat{W}_i(t, t + \tau) = \hat{x}_i(t + \tau)/\hat{x}_i(t)$, for a prediction period $\tau = 60$ days and for post-BA.2 variants (Figure 4B). To compute the frequencies $x_i(t + \tau)$, we evaluate the fitness model at time t , using tracking data and parameter inference only up to that time (**STAR Methods**). We evaluate regional frequency trajectories of each clade at multiple time points, including periods of observed increase ($\hat{W} > 1$) and decrease ($\hat{W} < 1$). Predicted and observed frequency changes are seen to be strongly correlated (coefficient of determination $R^2 = 0.84$); frequency increase is correctly predicted in 142/182 cases, and decline is correctly predicted in 144/149 cases.

Next, we test whether the fitness model can flag new variants of concern at an early point of their frequency trajectory.

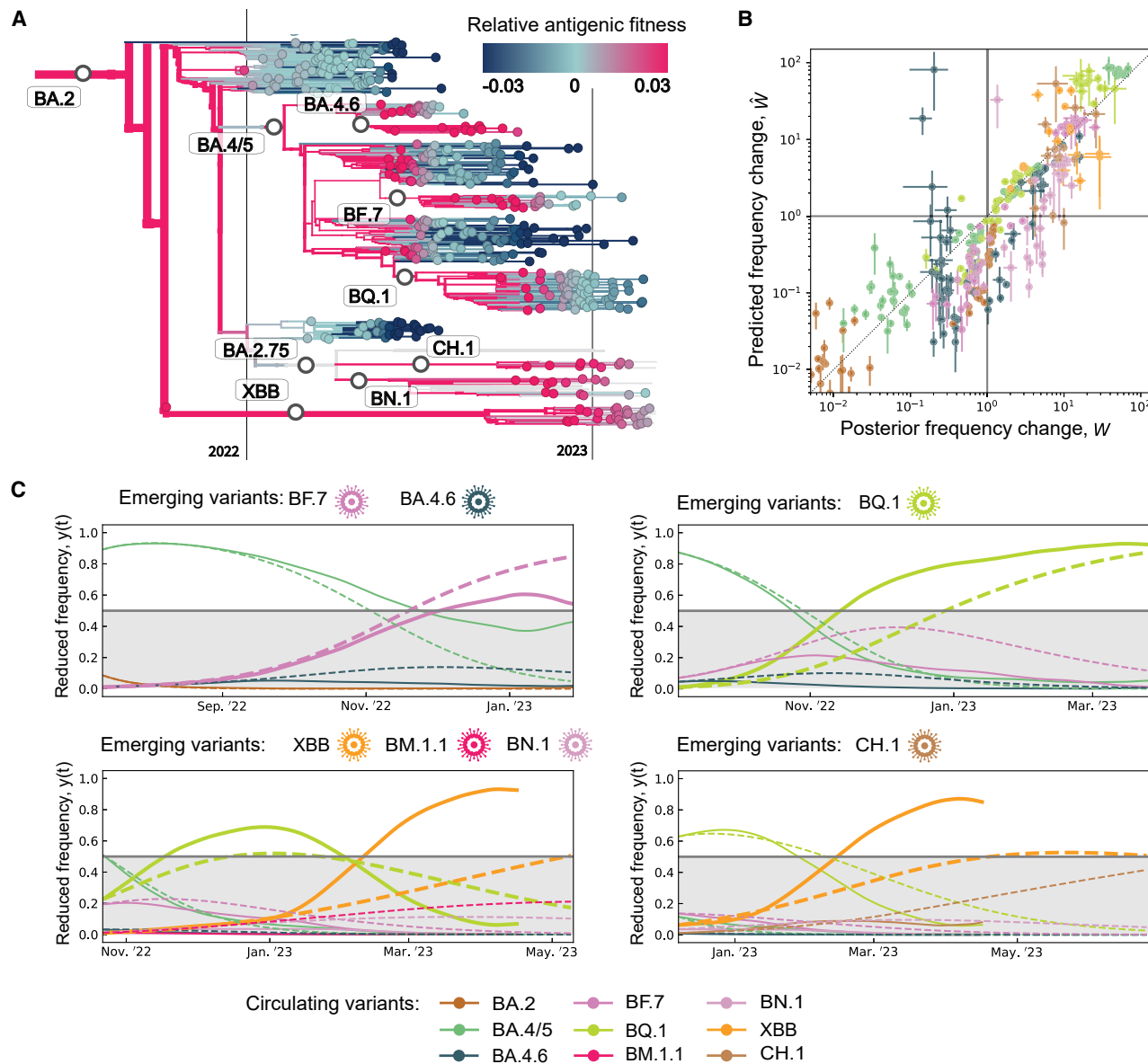


Figure 4. Predicting short-term evolution

(A) Strain tree of BA.2 and descendant variants; strains are colored by model-based clade- and time-dependent relative fitness, $f_i(t)$.
 (B) Short-term frequency change. We compare predicted changes, $W_i(t, t + \tau) = x_i(t + \tau)/\hat{x}_i(t)$, with posterior empirical changes, $\hat{W}_i(t, t + \tau) = \hat{x}_i(t + \tau)/\hat{x}_i(t)$, over periods $\tau = 60$ days in all longitudinally tracked regions for 8 variants i with initial frequencies $\hat{x}_i = 0.01, 0.2, 0.4$ (ascending segments) and $\hat{x}_i/\hat{x}_{i,\max} = 1, 0.5, 0.25$ (descending segments). Error bars indicate one standard deviation.
 (C) Predominance shifts. We compare predicted and posterior trajectories of reduced fitness, $y_i(t)$ (dashed) and $\hat{y}_i(t)$ (solid), over periods $\tau = 200$ days, starting from the emergence of new variants (marked above each panel); see **STAR Methods**. Bold lines highlight variants predicted to outcompete all other variants co-existing at their time of emergence (i.e., to reach reduced frequencies $y > 0.5$).

Whenever a new variant emerges at global frequency $\hat{x} = 0.01$, we predict its subsequent evolution in a window of 200 days together with all variants present at the start of prediction with frequency > 0.005 (**STAR Methods**). Figure 4C shows reduced frequency trajectories, $y_i(t)$, which are defined in these sets of competing variants. We compute predicted trajectories (dashed lines) from the antigenic fitness model at the start of each window, using tracking data and parameter inference only up to

that time, and compare them to empirical trajectories tracked from posterior data (solid lines). Of 7 variants with available antigenic data, BF.7, BQ.1, and XBB are correctly predicted to outcompete all variants present at the time of their emergence, i.e., to reach reduced frequencies > 0.5 , within 200 days. The other 4 variants are correctly predicted to remain below majority within that time interval. We note that XBB shows a pronounced fitness increase two months after emergence. This can be traced

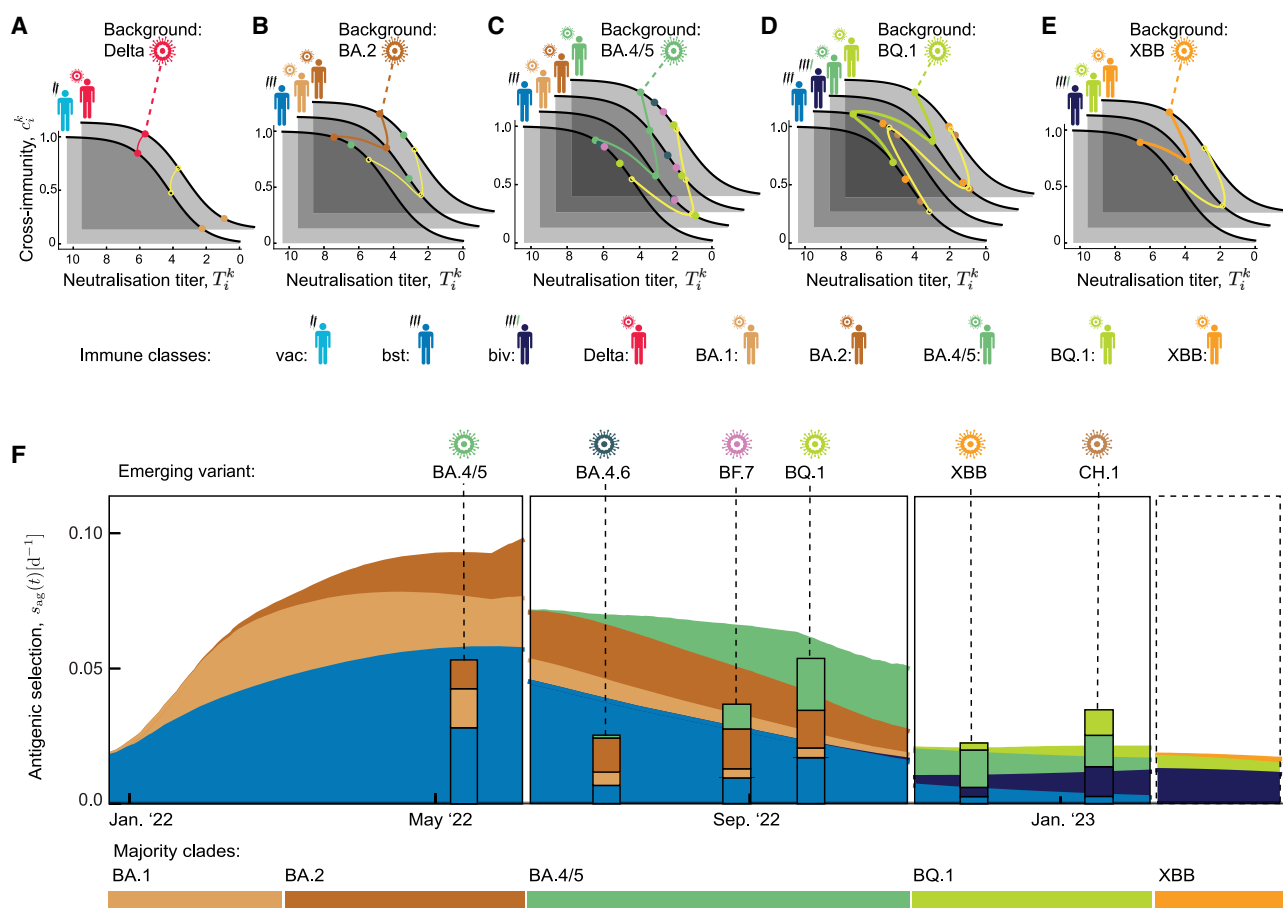


Figure 5. Antigenic selection profiles constrain emerging variants

(A–E) Antigenic landscapes. Each family of landscapes shows neutralization titers and cross-immunity factors, (T_i^k, c_i^k) (dots), for a given majority variant as antigenic background and competing minority variants in all immune classes relevant for the next clade shift. Yellow circles mark a “standard” mutant, as described in the text; data of the background variant and the standard mutant are joined by lines.

(F) Antigenic selection profiles. Predicted antigenic selection trajectories of the standard variant against the background majority variant and their breakdown into immune classes, $s_{ag}(t) = \sum_k s_k(t)$ (stacked areas), are shown for successive background variants (horizontal color bars). Posterior selection profiles of observed variants are shown at their time of emergence (stacked bars). The last panel shows the predicted profile for the future clade shift away from XBB.

to the subclade XBB.1.5 with the additional intrinsic change S:S486P, which increases ACE2 binding.⁵⁴ Continuously updated predictions on SARS-CoV-2 can be found at <https://previr.app>.

Selection windows and antigenic profiles of new variants

The preceding analysis predicts predominance changes in a set of variants coexisting at the start of prediction, but it remains agnostic about variants that emerge later. The genetic identity of new variants is highly stochastic and unlikely to be predictable.⁵⁵ However, the antigenic characteristics of successful variants are constrained by the history of previous infections and vaccinations. According to our fitness model, temporally localized windows of strong antigenic selection are generated when high population immunity coincides with high expected loss of cross-immunity on the steep flank of a Hill landscape in one or more immune classes.

To exploit this constraint for predictions, we first display the antigenic evolution on cross-immunity landscapes (Figures 5A–5E). For each of the major variants Delta, BA.1/2, BA.4/5, BQ.1, and XBB as antigenic background, a family of landscapes maps the titer T and the cross-immunity factor $c = H(T)$ for the background major variant and the competing minor variants (colored dots) in all immune classes relevant for the next evolutionary step. Here, we treat the antigenically similar variants BA.1 and BA.2 as a single antigenic background (Table S1). From these landscapes, we can read off the class-specific antigenic advance or titer drop, ΔT , and the resulting incremental escape from cross-immunity, Δc , of each competing variant compared to the background variant. A hypothetical “standard” mutant with a uniform $\Delta T = 2$ against the background variant is marked by yellow circles; this antigenic advance is close to the average of observed mutants. In the post-BA.2 period (see Figure 4), we compute the resulting antigenic selection profile, i.e., the time-dependent selection coefficient and its

breakdown into immune classes, for the standard mutant against the successive major variants (Figure 5F, shaded areas). This reveals a strongly time-dependent pattern: selection in a given immune class builds up by recent infections or vaccinations, and then it gets depleted by immune waning and even more rapidly by the shift to a new major variant that has largely completed the immune escape in that class.

The antigenic selection profiles of Figure 5B predict antigenic characteristics of new, yet unseen variants that can successfully escape population immunity. The predicted profile is conditional on the new variant's emergence at time t ; the computation uses tracking and antigenic data up to that time. Remarkably, the observed profiles of new high-fitness variants at their actual time of emergence are in broad agreement with the predicted pattern (Figure 5F, stacked bars); that is, the overall amplitude and the directions of antigenic escape evolution are constrained by selection computable from prior data. Three immune classes, booster vaccinations and infections by BA.1 and BA.2, drive the antigenic shift BA.2–BA.4/5. Primary vaccinations are no longer relevant for this shift because BA.1 and BA.2 have already largely completed the immune escape in this class (Figure 5A). The variant BA.4/5 escapes only partially in the classes BA.1/2 and bst. Hence, these classes remain relevant for the variants emerging on the antigenic background of BA.4/5, including BA.4.6, BF.7, and BQ.1, while selection induced by BA.4/5 infections is building up. This class, together with BQ.1 infections and bivalent booster vaccinations, governs the following variants XBB and CH.1, which emerge on the antigenic background of BQ.1.

All of these post-BA.4/5 variants show pronounced convergent evolution in few epitope sites; this canalization of genome evolution has been linked to immune imprinting from previous infections or vaccinations.¹⁰ Escape effects of such mutations, as measured by deep mutational scanning (DMS), can serve as input to our antigenic selection profiles and growth predictions (STAR Methods). Specifically, the post-BA.4/5 variants differ from their recent ancestor BA.4/5 in up to 6 point mutations in the receptor binding domain, some of which show large escape effects from BA.4/5 breakthrough infections.¹⁰ These effects explain the large antigenic advance of BQ.1 in immune class $k = \text{BA.4/5}$ (Figure 5C) and the resulting fitness advantage against the competing strains BA.4.6 and BF.7 (Figure 4C). However, the initial antigenic advance and the resulting fitness gain of the recombinant variant XBB against BQ.1 (Figures 5D and 4C) is larger than expected from the sum of DMS escape effects of its point mutations (STAR Methods).

The next shift, which will take place from an XBB background, is predicted to be driven by bivalent booster vaccinations, BQ.1 infections, and a smaller component of XBB infections reflecting reduced case numbers (Figure 5E). We note that the predicted profiles list the spectrum of immune classes inducing selection for new variants. Given the increasing differentiation of population immunity, we also expect variants that carry antigenic change in some but not all of these classes.

DISCUSSION

Here, we have established a data-driven multi-component fitness model for the evolution of SARS-CoV-2. The model es-

tablishes a computable cross-scale analysis of how immunity shapes evolution: molecular interactions between protective antibodies and the viral proteins, measured by neutralization assays, govern the immune protection of individuals^{11,12}; cross-immunity data, together with epidemiological and sequence data, can be scaled up to population immunity; and trajectories of population immunity shape fitness seascapes on which viral variants compete for evolutionary success. By applying this model to tracked evolutionary trajectories in multiple regions, we have quantified intrinsic and antigenic selection driving the genetic and functional evolution of SARS-CoV-2. In particular, primary vaccination impacted the speed of global clade shifts in 2021; booster vaccination provided higher cross-protection in the same period but generated significant selection for antigenic escape only several months later (Figure 3). These results underscore that vaccine breadth is important for constraining antigenic escape evolution. More broadly, they highlight the need to integrate evolutionary feedback into vaccine design.

Three global trends in the recent evolution of SARS-CoV-2 are revealed by our analysis. First, antigenic selection has increased in relative strength and has broadened its target. That is, primary infection by distinct viral variants has generated an increasing number of immune classes and antigenic selection components; in parallel, multiple competing antigenic variants have appeared in recent shifts (Figures 3 and 5). Second, intrinsic selection has broadly decreased in strength, and some compensatory intrinsic changes have been reported.⁵⁶ Third, the overall speed of clade shifts has decreased substantially since the peak of the pandemic. These trends mark the transition from initial post-zoonotic adaptation of the virus to evolution in a well-adapted endemic state. A plausible endpoint of this transition becomes clear by comparison with influenza, a long-term endemic virus in humans. The evolution of influenza is a continuous adaptive process driven by antigenic selection, where multiple variants with different antigenic profiles compete for predominance.⁵⁷ In contrast, non-antigenic mutations in influenza proteins are under broad negative selection; observed changes often compensate the deleterious collateral effects of antigenic evolution on conserved molecular traits, including protein stability and receptor binding.^{55,57,58}

Looking forward, our analysis establishes methods to predict the short-term evolution of SARS-CoV-2. The antigenic fitness model predicts how likely emerging variants will rise to predominance in the population of circulating strains, provided cross-immunity data for these variants are available at the time of prediction (Figure 4). Antigenic selection profiles for new variants, which build up and can be computed even prior to their emergence, constrain the directions of likely antigenic evolution (Figure 5). Such profiles can serve to identify informative immune cohorts for antigenic surveillance by neutralization tests. Deep mutational scanning^{10,59} and high-throughput *in vitro* evolution^{56,60} have recently been established to map the genetic profile of SARS-CoV-2 evolution, including the genomic distribution of likely escape mutations as well as their antigenic and receptor binding effects. These approaches may eventually provide genotype-phenotype maps for antigenic evolution.⁶¹ Combined with our population-level antigenic selection profiles,

such data can further constrain the likely paths of escape from human immunity.

In a broader context, our results show how the coupled dynamics of human population immunity and viral evolution can be digested into predictions for global pathogens. The approach addresses a notorious problem: sequence-based data of the evolving pathogen alone, including the genetic changes and the initial growth rates of emerging mutants, provide only limited information on their eventual fixation and evolutionary impact.^{57,62} This is because antigenic escape evolution is complex: a given escape mutation has a spectrum of effects in multiple classes of population immunity (Figure 5). Within each class, selection is epistatic and time-dependent: pressure for escape peaks on the steep flanks of cross-immunity Hill functions, and its strength is modulated by new infections or vaccinations and by immune waning. We have shown that immune selection is computable despite this complexity, given integrated molecular and epidemiological data. Thus, our analysis calls for continued, comprehensive surveillance of SARS-CoV-2, combining tracking of genome sequences and incidence data with timely cross-immunity analysis. This input will be critical for our ability to predict antigenic escape evolution and to harvest such predictions for preemptive vaccine design.

Limitations of the study

Our analysis uses population immunity trajectories inferred by combined tracking of epidemiological, sequence, and cross-immunity data. Undersampling or biases in any of these source data limit the accuracy of the inference. Sequencing biases between clades also affect the inference of empirical fitness. To mitigate these effects, the longitudinal analysis is carried out in a set of 13 regions with comparable data quality (selection criteria are detailed in **STAR Methods**). Hence, the breakdown of selection components applies to the set of regions accessible to our analysis; the availability of comparable data precludes a fully global model-based inference of selection. Data on cross-immunity between viral variants is aggregated from multiple studies (**STAR Methods**; **Table S4**). Biases and sensitivity differences between datasets propagate into the model-based fitness differences between viral variants.

The minimal fitness model uses a simplified representation of immune classes, enabling the use of available neutralization data for cross-scale analysis of population immunity. The model effectively averages over the variation of cross-immunity between human hosts within the same immune class and neglects correlations between multiple infections. In particular, as noted above, this treatment assumes that host-to-host differences in immunodominance, antigenic shift, or immune waning have only limited impact on global antigenic selection and the resulting evolutionary dynamics. Furthermore, our fitness model is derived from an underlying multi-strain epidemiological model under specific assumptions, which decouple relative fitness from absolute growth and imply additivity of antigenic and intrinsic fitness components. These assumptions are detailed in **STAR Methods**; see also **Figure S3** for validity checks and error margins of the selection-growth decoupling.

Our predictive analysis leverages population immunity derived from past data to signal near-future prevalence shifts between variants and to constrain antigenic profiles of emerging variants. Antigenic surveillance is the main limiting factor of these and future evolutionary predictions. More dense and timely antigenic data are required to fully assess and harvest the predictive power of the fitness model. Furthermore, a comprehensive statistical validation will require longer time series of tracked evolutionary data.

STAR METHODS

Detailed methods are provided in the online version of this paper and include the following:

- **KEY RESOURCES TABLE**
- **RESOURCE AVAILABILITY**
 - Lead contact
 - Materials availability
 - Data and code availability
- **METHOD DETAILS**
 - Antigenic data
 - Sequence data and primary sequence analysis
 - Frequency trajectories of variants
 - Infection and vaccination trajectories
 - Data integration for regional analysis
 - Inference of empirical fitness
 - Cross-immunity trajectories
 - Minimal fitness model
 - Model validation
 - Non-pharmaceutical interventions
 - Inference of fitness model parameters and selection coefficients
 - Significance analysis of the fitness model
 - Prediction of frequency trajectories
 - Antigenic selection profiles
- **QUANTIFICATION AND STATISTICAL ANALYSIS**

SUPPLEMENTAL INFORMATION

Supplemental information can be found online at <https://doi.org/10.1016/j.cell.2023.09.022>.

ACKNOWLEDGMENTS

We thank Florian Klein and Kanika Vanshylla for discussions. This work has been supported by Deutsche Forschungsgemeinschaft Grant SFB1310 (M.M., D.R., J.E., and M. Lässig). M. Łuksza is a Pew Biomedical Scholar and was partially supported by the Centers of Excellence for Influenza Research and Response (CEIRR, contract #75N93021C00014).

AUTHOR CONTRIBUTIONS

M.M. and M. Lässig conceived the project and developed methods. All authors analyzed data and contributed to writing the paper.

DECLARATION OF INTERESTS

The authors declare no competing interests.

Received: December 2, 2022

Revised: August 26, 2023

Accepted: September 21, 2023

Published: October 23, 2023

REFERENCES

1. Ozono, S., Zhang, Y., Ode, H., Sano, K., Tan, T.S., Imai, K., Miyoshi, K., Kishigami, S., Ueno, T., Iwatani, Y., et al. (2021). SARS-CoV-2 D614G spike mutation increases entry efficiency with enhanced ACE2-binding affinity. *Nat. Commun.* 12, 848. <https://doi.org/10.1038/s41467-021-21118-2>.
2. Meng, B., Kemp, S.A., Papa, G., Datir, R., Ferreira, I.A.T.M., Marelli, S., Harvey, W.T., Lytras, S., Mohamed, A., Gallo, G., et al. (2021). Recurrent emergence of SARS-CoV-2 spike deletion H69/V70 and its role in the Alpha variant B.1.1.7. *Cell Rep.* 35, 109292. <https://doi.org/10.1016/j.celrep.2021.109292>.
3. Mlcochova, P., Kemp, S.A., Dhar, M.S., Papa, G., Meng, B., Ferreira, I.A.T.M., Datir, R., Collier, D.A., Albecka, A., Singh, S., et al. (2021). SARS-CoV-2 B.1.617.2 Delta variant replication and immune evasion. *Nature* 599, 114–119. <https://doi.org/10.1038/s41586-021-03944-y>.
4. Wrobel, A.G., Benton, D.J., Xu, P., Roustan, C., Martin, S.R., Rosenthal, P.B., Skehel, J.J., and Gamblin, S.J. (2020). SARS-CoV-2 and bat RaTG13 spike glycoprotein structures inform on virus evolution and furin-cleavage effects. *Nat. Struct. Mol. Biol.* 27, 763–767. <https://doi.org/10.1038/s41594-020-0468-7>.
5. Gobeil, S.M.-C., Henderson, R., Stalls, V., Janowska, K., Huang, X., May, A., Speakman, M., Beaudoin, E., Manne, K., Li, D., et al. (2022). Structural diversity of the sars-cov-2 omicron spike. *Mol. Cell* 82, 2050–2068.e6. <https://doi.org/10.1016/j.molcel.2022.03.028>.
6. Harvey, W.T., Carabelli, A.M., Jackson, B., Gupta, R.K., Thomson, E.C., Harrison, E.M., Ludden, C., Reeve, R., Rambaut, A., et al.; COVID-19 Genomics UK COG-UK Consortium (2021). SARS-CoV-2 variants, spike mutations and immune escape. *Nat. Rev. Microbiol.* 19, 409–424. <https://doi.org/10.1038/s41579-021-00573-0>.
7. Planas, D., Veyer, D., Baidaliuk, A., Staropoli, I., Guivel-Benhassine, F., Rajah, M.M., Planchais, C., Porrot, F., Robillard, N., Puech, J., et al. (2021). Reduced sensitivity of SARS-CoV-2 variant Delta to antibody neutralization. *Nature* 596, 276–280. <https://doi.org/10.1038/s41586-021-03777-9>.
8. Planas, D., Saunders, N., Maes, P., Guivel-Benhassine, F., Planchais, C., Buchrieser, J., Bolland, W.H., Porrot, F., Staropoli, I., Lemoine, F., et al. (2022). Considerable escape of SARS-CoV-2 Omicron to antibody neutralization. *Nature* 602, 671–675. <https://doi.org/10.1038/s41586-021-04389-z>.
9. Garcia-Beltran, W.F., St Denis, K.J., Hoelzemer, A., Lam, E.C., Nitido, A.D., Sheehan, M.L., Berrios, C., Ofoman, O., Chang, C.C., Hauser, B.M., et al. (2022). mRNA-based COVID-19 vaccine boosters induce neutralizing immunity against SARS-CoV-2 Omicron variant. *Cell* 185, 457–466.e4. <https://doi.org/10.1016/j.cell.2021.12.033>.
10. Cao, Y., Jian, F., Wang, J., Yu, Y., Song, W., Yismayil, A., Wang, J., An, R., Chen, X., Zhang, N., et al. (2023). Imprinted SARS-CoV-2 humoral immunity induces convergent Omicron RBD evolution. *Nature* 614, 521–529. <https://doi.org/10.1038/s41586-022-05644-7>.
11. Khoury, D.S., Cromer, D., Reynaldi, A., Schlub, T.E., Wheatley, A.K., Juno, J.A., Subbarao, K., Kent, S.J., Triccas, J.A., and Davenport, M.P. (2021). Neutralizing antibody levels are highly predictive of immune protection from symptomatic SARS-CoV-2 infection. *Nat. Med.* 27, 1205–1211. <https://doi.org/10.1038/s41591-021-01377-8>.
12. Feng, S., Phillips, D.J., White, T., Sayal, H., Aley, P.K., Bibi, S., Dold, C., Fuskova, M., Gilbert, S.C., Hirsch, I., et al. (2021). Correlates of protection against symptomatic and asymptomatic SARS-CoV-2 infection. *Nat. Med.* 27, 2032–2040. <https://doi.org/10.1038/s41591-021-01540-1>.
13. Tracking SARS-CoV-2 variants. <https://www.who.int/en/activities/tracking-SARS-CoV-2-variants>
14. Davies, N.G., Abbott, S., Barnard, R.C., Jarvis, C.I., Kucharski, A.J., Munday, J.D., Pearson, C.A.B., Russell, T.W., Tully, D.C., Washburne, A.D., et al. (2021). Estimated transmissibility and impact of SARS-CoV-2 lineage B.1.1.7 in England. *Science* 372, eabg3055. <https://doi.org/10.1126/science.abg3055>.
15. Dhar, M.S., Marwal, R., Vs, R., Ponnusamy, K., Jolly, B., Bhoyer, R.C., Sardana, V., Naushin, S., Rophina, M., Mellan, T.A., et al. (2021). Genomic characterization and epidemiology of an emerging SARS-CoV-2 variant in Delhi, India. *Science* 374, 995–999. <https://doi.org/10.1126/science.abj9932>.
16. Kepler, L., Hamins-Puertolas, M., and Rasmussen, D.A. (2021). Decomposing the sources of SARS-CoV-2 fitness variation in the united states. *Virus Evol.* 7, veab073. <https://doi.org/10.1093/ve/veab073>.
17. Ulrich, L., Halwe, N.J., Taddeo, A., Ebert, N., Schön, J., Devisme, C., Trüeb, B.S., Hoffmann, B., Wider, M., Fan, X., et al. (2022). Enhanced fitness of SARS-CoV-2 variant of concern Alpha but not Beta. *Nature* 602, 307–313. <https://doi.org/10.1038/s41586-021-04342-0>.
18. Grenfell, B.T., Pybus, O.G., Gog, J.R., Wood, J.L.N., Daly, J.M., Mumford, J.A., and Holmes, E.C. (2004). Unifying the epidemiological and evolutionary dynamics of pathogens. *Science* 303, 327–332. <https://doi.org/10.1126/science.1090727>.
19. Reilla, S.A., Kulikova, Y.A., Dermitzakis, E.T., and Kondrashov, F.A. (2021). Rates of SARS-CoV-2 transmission and vaccination impact the fate of vaccine-resistant strains. *Sci. Rep.* 11, 15729. <https://doi.org/10.1038/s41598-021-95025-3>.
20. Saad-Roy, C.M., Morris, S.E., Metcalf, C.J.E., Mina, M.J., Baker, R.E., Farrar, J., Holmes, E.C., Pybus, O.G., Graham, A.L., Levin, S.A., et al. (2021). Epidemiological and evolutionary considerations of SARS-CoV-2 vaccine dosing regimes. *Science* 372, 363–370. <https://doi.org/10.1126/science.abg8663>.
21. Lobinska, G., Pauzner, A., Traulsen, A., Pilpel, Y., and Nowak, M.A. (2022). Evolution of resistance to covid-19 vaccination with dynamic social distancing. *Nat. Hum. Behav.* 6, 193–206. <https://doi.org/10.1038/s41562-021-01281-8L>.
22. Łukasz, M., and Lässig, M. (2014). A predictive fitness model for influenza. *Nature* 507, 57–61. <https://doi.org/10.1038/nature13087>.
23. Wen, F.T., Malani, A., and Cobey, S. (2022). The potential beneficial effects of vaccination on antigenically evolving pathogens. *Am. Nat.* 199, 223–237. <https://doi.org/10.1086/717410>.
24. Wen, F.T., Bell, S.M., Bedford, T., and Cobey, S. (2018). Estimating vaccine-driven selection in seasonal influenza. *Viruses* 10, 509. <https://doi.org/10.3390/v10090509>.
25. Mathieu, E., Ritchie, H., Rodés-Guirao, L., Appel, C., Giattino, C., Hasell, J., Macdonald, B., Dattani, S., Beltekian, D., Ortiz-Ospina, E., and Roser, M. (2020). Coronavirus Pandemic (COVID-19) (OurWorldInData.org). <https://ourworldindata.org/coronavirus>.
26. Centers for Disease Control and Prevention (2023). COVID Data Tracker (U.S. Department of Health and Human Services, CDC). <https://covid.cdc.gov/covid-data-tracker>.
27. Shu, Y., and McCauley, J. (2017). GISAID: Global initiative on sharing all influenza data – from vision to reality. *Euro Surveill.* 22, 30494. <https://doi.org/10.2807/1560-7917.ES.2017.22.13.30494>.
28. Gangavarapu, K., Latif, A.A., Mullen, J.L., Alkuzweny, M., Hufbauer, E., Tsueng, G., Haag, E., Zeller, M., Aceves, C.M., Zalets, K., et al. (2023). Outbreak.info genomic reports: scalable and dynamics surveillance of SARS-CoV-2 variants and mutations. *Nat. Methods* 20, 512–522.
29. Van der Straten, K., Guerra, D., van Gils, M.J., Bontjer, I., Caniels, T.G., van Willigen, H.D.G., Wynberg, E., Poniman, M., Burger, J.A., Bouhuys, J.H., et al. (2022). Antigenic cartography using sera from sequence-confirmed SARS-CoV-2 variants of concern infections reveals antigenic divergence

- of Omicron. *Immunity* 55, 1725–1731.e4. <https://doi.org/10.1016/j.imuni.2022.07.018>.
30. Wilks, S.H., Mühlmann, B., Shen, X., Türell, S., Legresley, E.B., Netzl, A., Caniza, M.A., Chacaltana-Huarcaya, J.N., Corman, V.M., Daniell, X., et al. (2023). Mapping SARS-CoV-2 antigenic relationships and serological responses. Preprint at bioRxiv. <https://doi.org/10.1101/2022.01.28.477987>.
31. Wang, Q., Iketani, S., Li, Z., Liu, L., Guo, Y., Huang, Y., Bowen, A.D., Liu, M., Wang, M., Yu, J., et al. (2023). Alarming antibody evasion properties of rising sars-cov-2 bq and xbb subvariants. *Cell* 186, 279–286.e8. <https://doi.org/10.1016/j.cell.2022.12.018>.
32. Davis-Gardner, M.E., Lai, L., Wall, B., Samaha, H., Solis, D., Lee, M., Porter-Morrison, A., Hentenaar, I.T., Yamamoto, F., Godbole, S., et al. (2023). Neutralization against ba.2.75.2, bq.1.1, and xbb from mrna bivalent booster. *N. Engl. J. Med.* 388, 183–185. <https://doi.org/10.1056/NEJMcp2214293>.
33. Coudeville, L., Bailleux, F., Riche, B., Megas, F., Andre, P., and Ecochard, R. (2010). Relationship between haemagglutination-inhibiting antibody titres and clinical protection against influenza: development and application of a bayesian random-effects model. *BMC Med. Res. Methodol.* 10, 18. <https://doi.org/10.1186/1471-2288-10-18>.
34. Dunning, A.J., DiazGranados, C.A., Voloshen, T., Hu, B., Landolfi, V.A., and Talbot, H.K. (2016). Correlates of protection against influenza in the elderly: Results from an influenza vaccine efficacy trial. *Clin. Vaccine Immunol.* 23, 228–235. <https://doi.org/10.1128/CVI.00604-15>.
35. Rotem, A., Serohijos, A.W.R., Chang, C.B., Wolfe, J.T., Fischer, A.E., Mekhora, T.S., Zhang, H., Tao, Y., Lloyd Ung, W., Choi, J.M., et al. (2018). Evolution on the biophysical fitness landscape of an rna virus. *Mol. Biol. Evol.* 35, 2390–2400. <https://doi.org/10.1093/molbev/msy131>.
36. Meijers, M., Vanshylla, K., Gruell, H., Klein, F., and Lässig, M. (2021). Predicting in vivo escape dynamics of HIV-1 from a broadly neutralizing antibody. *Proc. Natl. Acad. Sci. USA* 118, e2104651118. <https://doi.org/10.1073/pnas.2104651118>.
37. Iyer, A.S., Jones, F.K., Nodoushani, A., Kelly, M., Becker, M., Slater, D., Mills, R., Teng, E., Kamruzzaman, M., Garcia-Beltran, W.F., et al. (2020). Persistence and decay of human antibody responses to the receptor binding domain of SARS-CoV-2 spike protein in COVID-19 patients. *Sci. Immunol.* 5, eabe0367. <https://doi.org/10.1126/sciimmunol.abe0367>.
38. Israel, A., Shenhav, Y., Green, I., Merzon, E., Golan-cohen, A., Schäffer, A.A., Ruppin, E., Vinker, S., and Magen, E. (2021). Large-scale study of antibody titer decay following BNT162b2 mRNA vaccine or SARS-CoV-2 infection. *Vaccines* 10, 64. <https://doi.org/10.3390/vaccines10010064>.
39. Park, S.W., Champredon, D., Weitz, J.S., and Dushoff, J. (2019). A practical generation-interval-based approach to inferring the strength of epidemic from their speed. *Epidemics* 27, 12–18. <https://doi.org/10.1016/j.epidem.2018.12.002>.
40. Park, S.W., Bolker, B.M., Funk, S., Metcalf, C.J.E., Weitz, J.S., Grenfell, B.T., and Dushoff, J. (2022). The importance of the generation interval in investigating dynamics and control of new SARS-CoV-2 variants. *J. R. Soc. Interface* 19, 20220173. <https://doi.org/10.1098/rsif.2022.0173>.
41. Morris, D.H., Gostic, K.M., Pompei, S., Bedford, T., Łukaszka, M., Neher, R.A., Grenfell, B.T., Lässig, M., and McCauley, J.W. (2018). Predictive modeling of influenza shows the promise of applied evolutionary biology. *Trends Microbiol.* 26, 102–118. <https://doi.org/10.1016/j.tim.2017.09.004>.
42. Huddleston, J., Barnes, J.R., Rowe, T., Xu, X., Kondor, R., Wentworth, D.E., Whittaker, L., Ermetal, B., Daniels, R.S., McCauley, J.W., et al. (2020). Integrating genotypes and phenotypes improves long-term forecasts of seasonal influenza A/H3N2 evolution. *Elife* 9, e60067. <https://doi.org/10.7554/elife.60067>.
43. Andreasen, V., Lin, J., and Levin, S.A. (1997). The dynamics of cocirculating influenza strains conferring partial cross-immunity. *J. Math. Biol.* 35, 825–842. <https://doi.org/10.1007/s002850050079>.
44. Gog, J.R., and Swinton, J. (2002). A status-based approach to multiple strain dynamics. *J. Math. Biol.* 44, 169–184. <https://doi.org/10.1007/s002850100120>.
45. Gog, J.R., and Grenfell, B.T. (2002). Dynamics and selection of many-strain pathogens. *Proc. Natl. Acad. Sci. USA* 99, 17209–17214. <https://doi.org/10.1073/pnas.252512799>.
46. Lee, J.M., Eguia, R., Zost, S.J., Choudhary, S., Wilson, P.C., Bedford, T., Stevens-Ayers, T., Boeckh, M., Hurt, A.C., Lakdawala, S.S., et al. (2019). Mapping person-to-person variation in viral mutations that escape polyclonal serum targeting influenza hemagglutinin. *Elife* 8, e49324. <https://doi.org/10.7554/elife.49324>.
47. Cobey, S., and Hensley, S.E. (2017). Immune history and influenza virus susceptibility. *Curr. Opin. Virol.* 22, 105–111. <https://doi.org/10.1016/j.coviro.2016.12.004>.
48. Bates, T.A., McBride, S.K., Leier, H.C., Guzman, G., Lyski, Z.L., Schoen, D., Winders, B., Lee, J.-Y., Lee, D.X., Messer, W.B., et al. (2022). Vaccination before or after SARS-CoV-2 infection leads to robust humoral response and antibodies that effectively neutralize variants. *Sci. Immunol.* 7, eabn8014. <https://doi.org/10.1126/sciimmunol.abn8014>.
49. Hart, W.S., Miller, E., Andrews, N.J., Waight, P., Maini, P.K., Funk, S., and Thompson, R.N. (2022). Generation time of the alpha and delta SARS-CoV-2 variants: an epidemiological analysis. *Lancet Infect. Dis.* 22, 603–610. [https://doi.org/10.1016/S1473-3099\(22\)00001-9](https://doi.org/10.1016/S1473-3099(22)00001-9).
50. Park, S.W., Sun, K., Abbott, S., Sender, R., Bar-On, Y.M., Weitz, J.S., Funk, S., Grenfell, B.T., Backer, J.A., Wallinga, J., et al. (2023). Inferring the differences in incubation-period and generation-interval distributions of the Delta and Omicron variants of SARS-CoV-2. *Proc. Natl. Acad. Sci. USA* 120, e2221887120. <https://doi.org/10.1073/pnas.2221887120>.
51. Yuan, S., Ye, Z.-W., Liang, R., Tang, K., Zhang, A.J., Lu, G., Ong, C.P., Man Poon, V.K., Chan, C.C.-S., Mok, B.W.-Y., et al. (2022). Pathogenicity, transmissibility, and fitness of SARS-CoV-2 Omicron in Syrian hamsters. *Science* 377, 428–433. <https://doi.org/10.1126/science.abn8939>.
52. Gruell, H., Vanshylla, K., Tober-Lau, P., Hillus, D., Schommers, P., Lehmann, C., Kurth, F., Sander, L.E., and Klein, F. (2022). mRNA booster immunization elicits potent neutralizing serum activity against the SARS-CoV-2 Omicron variant. *Nat. Med.* 28, 477–480. <https://doi.org/10.1038/s41591-021-01676-0>.
53. Hachmann, N.P., Miller, J., Collier, A.R.Y., Ventura, J.D., Yu, J., Rowe, M., Bondzie, E.A., Powers, O., Surve, N., Hall, K., et al. (2022). Neutralization escape by SARS-CoV-2 Omicron subvariants BA.2.12.1, BA.4, and BA.5. *N. Engl. J. Med.* 387, 86–88. <https://doi.org/10.1056/NEJMcp2206576>.
54. Yue, C., Song, W., Wang, L., Jian, F., Chen, X., Gao, F., Shen, Z., Wang, Y., Wang, X., and Cao, Y. (2023). ACE2 binding and antibody evasion in enhanced transmissibility of XBB.1.5. *Lancet* 323, 278–280. [https://doi.org/10.1016/S1473-3099\(23\)00010-5](https://doi.org/10.1016/S1473-3099(23)00010-5).
55. Lässig, M., Mustonen, V., and Walczak, A.M. (2017). Predicting evolution. *Nat. Ecol. Evol.* 1, 0077. <https://doi.org/10.1038/s41559-017-0077>.
56. Moulana, A., Dupic, T., Phillips, A.M., Chang, J., Nieves, S., Roffler, A.A., Greaney, A.J., Starr, T.N., Bloom, J.D., and Desai, M.M. (2022). Compensatory epistasis maintains ace2 affinity in sars-cov-2 omicron ba.1. *Nat. Commun.* 13, 7011. <https://doi.org/10.1038/s41467-022-34506-z>.
57. Strelkowa, N., and Lässig, M. (2012). Clonal interference in the evolution of influenza. *Genetics* 192, 671–682. <https://doi.org/10.1534/genetics.112.143396>.
58. Gong, L.I., Suchard, M.A., and Bloom, J.D. (2013). Stability-mediated epistasis constrains the evolution of an influenza protein. *Elife* 2, e00631. <https://doi.org/10.7554/elife.00631>.
59. Starr, T.N., Greaney, A.J., Stewart, C.M., Walls, A.C., Hannon, W.W., Veesler, D., and Bloom, J.D. (2022). Deep mutational scans for ACE2 binding, RBD expression, and antibody escape in the SARS-CoV-2 Omicron BA.1 and BA.2 receptor-binding domains. *PLoS Pathog.* 18, e1010951. <https://doi.org/10.1371/journal.ppat.1010951>.

60. Zahradník, J., Marciano, S., Shemesh, M., Zoler, E., Harari, D., Chiaravall, J., Meyer, B., Rudich, Y., Li, C., Marton, I., et al. (2021). SARS-CoV-2 variant prediction and antiviral drug design are enabled by RBD in vitro evolution. *Nat. Microbiol.* 6, 1188–1198. <https://doi.org/10.1038/s41564-021-00954-4>.
61. Moulana, A., Dupic, T., Phillips, A.M., and Desai, M.M. (2023). Genotype-phenotype landscapes for immune-pathogen coevolution. *Trends Immunol.* 44, 384–396. <https://doi.org/10.1016/j.it.2023.03.006>.
62. Barrat-Charlaix, P., Huddleston, J., Bedford, T., and Neher, R.A. (2021). Limited Predictability of Amino Acid Substitutions in Seasonal Influenza Viruses. *Mol. Biol. Evol.* 38, 2767–2777. <https://doi.org/10.1093/molbev/msab065>.
63. Wang, P., Nair, M.S., Liu, L., Iketani, S., Luo, Y., Guo, Y., Wang, M., Yu, J., Zhang, B., Kwong, P.D., et al. (2021). Antibody resistance of SARS-CoV-2 variants B.1.351 and B.1.1.7. *Nature* 593, 130–135. <https://doi.org/10.1038/s41586-021-03398-2>.
64. Liu, Y., Liu, J., Xia, H., Zhang, X., Zou, J., Fontes-Garfias, C.R., Weaver, S.C., Swanson, K.A., Cai, H., Sarkar, R., et al. (2021). BNT162b2-elicited neutralization against new SARS-CoV-2 spike variants. *N. Engl. J. Med.* 385, 472–474. <https://doi.org/10.1056/nejmci20106083>.
65. Planas, D., Bruel, T., Grzelak, L., Guivel-Benhassine, F., Staropoli, I., Portrot, F., Planchais, C., Buchrieser, J., Rajah, M.M., Bishop, E., et al. (2021). Sensitivity of infectious SARS-CoV-2 B.1.1.7 and B.1.351 variants to neutralizing antibodies. *Nat. Med.* 27, 917–924. <https://doi.org/10.1038/s41591-021-01318-5>.
66. Muik, A., Wallisch, A.-K., Sänger, B., Swanson, K.A., Mühl, J., Chen, W., Cai, H., Maurus, D., Sarkar, R., Türeci, Ö., et al. (2021). Neutralization of SARS-CoV-2 lineage B.1.1.7 pseudovirus by BNT162b2 vaccine-elicited human sera. *Science* 371, 1152–1153. <https://doi.org/10.1126/science.abg610>.
67. The CODA Collaborative, Kimura, I., Shirakawa, K., Takaori-Konda, A., Nakada, T., Kaneda, A., Nakagawa, S., and Sato, K. (2021). Neutralization of the sars-cov-2 mu variant by convalescent and vaccine serum. *N. Engl. J. Med. Overseas Ed.* 385, 2395–2397. <https://doi.org/10.1056/NEJMc2116018>.
68. Rössler, A., Riepler, L., Bante, D., von Laer, D., and Kimpel, J. (2022). SARS-CoV-2 Omicron variant neutralization in serum from vaccinated and convalescent persons. *N. Engl. J. Med.* 386, 698–700. <https://doi.org/10.1056/nejmci2119236>.
69. Iketani, S., Liu, L., Guo, Y., Liu, L., Chan, J.F.W., Huang, Y., Wang, M., Luo, Y., Yu, J., Chu, H., et al. (2022). Antibody evasion properties of SARS-CoV-2 Omicron sublineages. *Nature* 604, 553–556. <https://doi.org/10.1038/s41586-022-04594-4>.
70. Bowen, J.E., Sprouse, K.R., Walls, A.C., Mazzitelli, I.G., Logue, J.K., Franko, N.M., Ahmed, K., Shariq, A., Cameroni, E., Gori, A., et al. (2022). Omicron BA.1 and BA.2 neutralizing activity elicited by a comprehensive panel of human vaccines. Preprint at bioRxiv. <https://doi.org/10.1101/2022.03.15.484542>.
71. Cao, Y., Yisimayi, A., Jian, F., Song, W., Xiao, T., Wang, L., Du, S., Wang, J., Li, Q., Chen, X., et al. (2022). BA.2.12.1, BA.4 and BA.5 escape antibodies elicited by omicron infection. *Nature* 608, 593–602. <https://doi.org/10.1038/s41586-022-04980-y>.
72. Mykytyn, A.Z., Rissmann, M., Kok, A., Rosu, M.E., Schipper, D., Breugem, T.I., van den Doel, P.B., Chandler, F., Bestebroer, T., de Wit, M., et al. (2022). Antigenic cartography of SARS-CoV-2 reveals that Omicron BA.1 and BA.2 are antigenically distinct. *Sci. Immunol.* 7, eabq4450. <https://doi.org/10.1126/scimmunol.abq4450>.
73. Wang, Q., Guo, Y., Iketani, S., Nair, M.S., Li, Z., Mohri, H., Wang, M., Yu, J., Bowen, A.D., Chang, J.Y., et al. (2022). Antibody evasion by SARS-CoV-2 omicron subvariants BA.2.12.1, BA.4 and BA.5. *Nature* 608, 603–608. <https://doi.org/10.1038/s41586-022-05053-w>.
74. Qu, P., Faraone, J.N., Evans, J.P., Zheng, Y.-M., Carlin, C., Anghelina, M., Stevens, P., Fernandez, S., Jones, D., Panchal, A., et al. (2023). Extraordinary evasion of neutralizing antibody response by omicron XBB.1.5, CH.1.1 and CA.3.1 variants. Preprint at bioRxiv. <https://doi.org/10.1101/2023.01.16.524244>.
75. Kurhade, C., Zou, J., Xia, H., Liu, M., Chang, H.C., Ren, P., Xie, X., and Shi, P.Y. (2023). Low neutralization of SARS-CoV-2 omicron BA.2.75.2, BQ.1.1 and XBB.1 by parental mRNA vaccine or a BA.5 bivalent booster. *Nat. Med.* 29, 344–347. <https://doi.org/10.1038/s41591-022-02162-x>.
76. Jian, F., Yu, Y., Song, W., Yisimayi, A., Yu, L., Gao, Y., Zhang, N., Wang, Y., Shao, F., Hao, X., et al. (2022). Further humoral immunity evasion of emerging SARS-CoV-2 BA.4 and BA.5 subvariants. *Lancet Infect. Dis.* 22, 1535–1537. [https://doi.org/10.1016/S1473-3099\(22\)00642-9](https://doi.org/10.1016/S1473-3099(22)00642-9).
77. Wang, Q., Guo, Y., Tam, A.R., Valdez, R., Gordon, A., Liu, L., and Ho, D.D. (2023). Deep immunological imprinting due to the ancestral spike in the current bivalent covid-19 vaccine. Preprint at bioRxiv. <https://doi.org/10.1101/2023.05.03.539268>.
78. Neher, R.A., Bedford, T., Daniels, R.S., Russell, C.A., and Shraiman, B.I. (2016). Prediction, dynamics, and visualization of antigenic phenotypes of seasonal influenza viruses. *Proc. Natl. Acad. Sci. USA* 113, E1701–E1709. <https://doi.org/10.1073/pnas.1525578113>.
79. Polack, F.P., Thomas, S.J., Kitchin, N., Absalon, J., Gurtman, A., Lockhart, S., Perez, J.L., Pérez Marc, G., Moreira, E.D., Zerbini, C., et al. (2020). Safety and efficacy of the BNT162b2 mRNA Covid-19 vaccine. *N. Engl. J. Med.* 383, 2603–2615. <https://doi.org/10.1056/nejmoa2034577>.
80. Benson, D.A., Clark, K., Karsch-Mizrachi, I., Lipman, D.J., Ostell, J., and Sayers, E.W. (2015). GenBank. *Nucleic Acids Res.* 43, D30–D35. <https://doi.org/10.1093/nar/gku1216>.
81. Katoh, K., and Standley, D.M. (2013). MAFFT multiple sequence alignment software version 7: Improvements in performance and usability. *Mol. Biol. Evol.* 30, 772–780. <https://doi.org/10.1093/molbev/mst010>.
82. Minh, B.Q., Schmidt, H.A., Chernomor, O., Schrempf, D., Woodhams, M.D., von Haeseler, A., Lanfear, R., and Teeling, E. (2020). IQ-TREE 2: New models and efficient methods for phylogenetic inference in the genomic era. *Mol. Biol. Evol.* 37, 1530–1534. <https://doi.org/10.1093/molbev/msaa015>.
83. Hoang, D.T., Chernomor, O., von Haeseler, A., Minh, B.Q., Vinh, L.S., and Rosenberg, M.S. (2017). UFBoot2: Improving the ultrafast bootstrap approximation. *Mol. Biol. Evol.* 35, 518–522. <https://doi.org/10.5281/zenodo.854445>.
84. Smith, D.J., Lapedes, A.S., de Jong, J.C., Bestebroer, T.M., Rimmelzwaan, G.F., Osterhaus, A.D.M.E., and Fouchier, R.A.M. (2004). Mapping the antigenic and genetic evolution of influenza virus. *Science* 305, 371–376. <https://doi.org/10.1126/science.1097211>.
85. Bates, T.A., Leier, H.C., Lyski, Z.L., McBride, S.K., Coulter, F.J., Weinstein, J.B., Goodman, J.R., Lu, Z., Siegel, S.A.R., Sullivan, P., et al. (2021). Neutralization of SARS-CoV-2 variants by convalescent and BNT162b2 vaccinated serum. *Nat. Commun.* 12, 5135. <https://doi.org/10.1038/s41467-021-25479-6>.
86. Garcia-Beltran, W.F., Lam, E.C., St Denis, K., Nitido, A.D., Garcia, Z.H., Hauser, B.M., Feldman, J., Pavlovic, M.N., Gregory, D.J., Poznansky, M.C., et al. (2021). Multiple SARS-CoV-2 variants escape neutralization by vaccine-induced humoral immunity. *Cell* 184, 2372–2383.e9. <https://doi.org/10.1016/j.cell.2021.03.013>.
87. Smith, D.J., Forrest, S., Hightower, R.R., and Perelson, A.S. (1997). Deriving shape space parameters from immunological data. *J. Theor. Biol.* 189, 141–150.
88. Cameroni, E., Bowen, J.E., Rosen, L.E., Saliba, C., Zepeda, S.K., Culap, K., Pinto, D., VanBlargan, L.A., De Marco, A., di Julio, J., et al. (2022). Broadly neutralizing antibodies overcome sars-cov-2 omicron antigenic shift. *Nature* 602, 664–670. <https://doi.org/10.1038/s41586-021-04386-2>.
89. Khan, K., Karim, F., Ganga, Y., Bernstein, M., Jule, Z., Reedoy, K., Cele, S., Lustig, G., Amoako, D., Wolter, N., et al. (2022). Omicron BA.4/BA.5 escape neutralizing immunity elicited by ba.1 infection. *Nat. Commun.* 13, 4686. <https://doi.org/10.1038/s41467-022-32396-9>.

90. Liu, C., Ginn, H.M., Dejnirattisai, W., Supasa, P., Wang, B., Tuekprakhon, A., Nutalai, R., Zhou, D., Mentzer, A.J., Zhao, Y., et al. (2021). Reduced neutralization of SARS-CoV-2 B.1.617 by vaccine and convalescent serum. *Cell* 184, 4220–4236.e13. <https://doi.org/10.1016/j.cell.2021.06.020>.
91. Zhou, D., Dejnirattisai, W., Supasa, P., Liu, C., Mentzer, A.J., Ginn, H.M., Zhao, Y., Duyvesteyn, H.M.E., Tuekprakhon, A., Nutalai, R., et al. (2021). Evidence of escape of SARS-CoV-2 variant B.1.351 from natural and vaccine-induced sera. *Cell* 184, 2348–2361.e6. <https://doi.org/10.1016/j.cell.2021.02.037>.
92. Sagulenko, P., Puller, V., and Neher, R.A. (2018). TreeTime: Maximum-likelihood phylodynamic analysis. *Virus Evol.* 4, vex042. <https://doi.org/10.1093/ve/vex042>.
93. Kingman, J.F.C. (1982). The coalescent. *Stoch. Process. their Appl.* 13, 235–248. [https://doi.org/10.1016/0304-4149\(82\)90011-4](https://doi.org/10.1016/0304-4149(82)90011-4).
94. Hart, W.S., Abbott, S., Endo, A., Hellewell, J., Miller, E., Andrews, N., Maini, P.K., Funk, S., and Thompson, R.N. (2022). Inference of the SARS-CoV-2 generation time using UK household data. *Elife* 11, e70767. <https://doi.org/10.7554/elife.70767>.
95. Ali, S.T., Wang, L., Lau, E.H.Y., Xu, X.K., Du, Z., Wu, Y., Leung, G.M., Cowling, B.J., Zhang, Y., Ode, H., et al. (2020). Serial interval of SARS-CoV-2 was shortened over time by nonpharmaceutical interventions. *Science* 369, 1106–1109. <https://doi.org/10.1126/science.abc9004>.
96. Schwarz, G. (1978). Estimating the dimension of a model. *Ann. Statist.* 6, 461–464.

STAR★METHODS

KEY RESOURCES TABLE

REAGENT or RESOURCE	SOURCE	IDENTIFIER
Deposited data		
SARS-CoV-2 sequence data	GISAID EpiCov Database	http://www.gisaid.org
Infection and vaccination rates	Ourworldindata	https://www.ourworldindata.org
Infection and vaccination rates	CDC COVID Data Tracker	https://www.covid.cdc.gov/covid-data-tracker
Antigenic Data	See reference list ^{3,7,8,10,29–32,52,53,63–83}	Table S4
Software and algorithms		
MAFFT v7.490	Katoh and Standley ⁸⁴	https://mafft.cbrc.jp
IQTree	Minh et al. ⁸⁵	http://www.iqtree.org/
TreeTime	Sagulenko et al. ⁸⁶	https://github.com/neherlab/treetime

RESOURCE AVAILABILITY

Lead contact

Further information and requests for data should be directed to and will be fulfilled by the lead contact, Michael Lässig (mlaessig@uni-koeln.de).

Materials availability

This study did not generate new unique reagents, but raw data and code generated as part of this research can be found on public resources as specified in the [data and code availability](#) section below.

Data and code availability

- This paper analyzes existing, publicly available data. These accession numbers for the datasets are listed in the [key resources table](#).
- Results and analyses can be found at https://github.com/m-meijers/Population_Immunity_SARSCOV2 and are publicly available as of the date of publication. DOIs are listed in the [key resources table](#).
- Any additional information required to reanalyze the data reported in this paper is available from the [lead contact](#) upon request.

METHOD DETAILS

Antigenic data

Neutralisation assays for SARS-CoV-2 test the potency of antisera induced by a given primary immunisation to neutralise viruses of different variants. Log dilution titers measure the minimum antiserum concentration required for neutralisation,

$$T_i^k = \log_2 \frac{K_0}{K_i^k}, \quad (\text{Equation 4})$$

relative to a reference concentration K_0 . Hence, log₂ titer differences, or neutralisation fold changes, $\Delta T_{ij}^k \equiv \Delta T_j^k - T_i^k$, measure differences in antigenicity between variants, $\Delta T_{ij}^k = \log_2(K_j^k / K_i^k)$. We note that these differences are specific to a given primary infection or vaccination (immune class) k . For example, the inequality $T_{\text{AlphaDelta}}^{\text{bst}} < T_{\text{AlphaDelta}}^{\text{vac}}$ reflects the increased breadth of booster vaccinations compared to primary vaccinations. In contrast, uni-valued antigenic distances between variants, d_{ij} , can be computed from the titer matrix (T_i^k) by multi-dimensional scaling methods.^{84,87} Such distance measures average over inhomogeneities between immune classes. Here we define a matrix of titer drops ΔT_i^k ,

$$\Delta T_i^k = T_*^k - T_i^k \quad (i = \text{Alpha, Delta, ..., CH.1}; k = \text{Alpha, Delta, ..., XBB, vac, bst, biv}), \quad (\text{Equation 5})$$

with respect to a reference titer for each immune class, $T_*^k = T_1^k$ ($k = \text{Alpha, Delta, ..., XBB}$) and $T_*^k = T_1^k$ ($k = \text{vac, bst, biv}$). This procedure eliminates technical differences between assays in absolute antibody concentration. We assemble this matrix in [Table S1](#),

using primary data from different sources^{3,7,8,10,29–32,52,53,63–77,85,86,88–91} (see also **Table S4**). We proceed as follows: (i) For matrix elements with available data, ΔT_i^k is the average of the corresponding primary measurements. (ii) If no data are available for ΔT_i^k but the conjugate titer ΔT_k^i has been measured, we use the approximate substitution $\Delta T_i^k \approx \Delta T_k^i$, as discussed in Neher et al.⁷⁸ (iii) If no data are available for ΔT_i^k but the titer ΔT_j^k of a closely related clade has been measured, we use the approximate substitution $\Delta T_i^k \approx \Delta T_j^k$, which should be understood as a lower bound. Approximate substitutions are indicated by italics in **Table S1**.

The matrix of absolute neutralisation titers, T_i^k , is then computed by **Equation 5**, combining the titer drops ΔT_i^k of **Table S1** and the reference titers $T_*^k = 6.5$ ($k = \text{Alpha, Delta, BQ.1}$), $T_*^{\text{vac}} = 7.8$, $T_*^{\text{bst}} = T_*^{\text{biv}} = 9.8$ reported in Polack et al.⁷⁹ A titer difference between vaccination and booster, $T_*^{\text{bst}} - T_*^{\text{vac}} \approx 2.0$, has been observed in several studies.^{8,9,52} The resulting titers T_i^k are shown in **Table S1**; they enter the cross-immunity functions c_i^k and $C_i^k(t)$ defined below.

The decay of antibody concentration after primary immunisation has been characterised in recent work.^{37,38} Here we describe this effect by a linear titer reduction with time after primary challenge,

$$T_i^k(\Delta t) = T_i^k - \frac{\Delta t}{\tau}, \quad (\text{Equation 6})$$

corresponding to an exponential decay of antibody concentration, with a uniform decay time 90 days (i.e., half-life $\tau = 65$ d). This is broadly consistent with experimental data; we infer decay times in the range [60, 170] d from several studies.^{7,8,37,38,52} In addition, we check that varying τ in this range does not affect our results (in particular, the rank order of variants with respect to antigenic fitness remains unchanged).

Sequence data and primary sequence analysis

The study is based on sequence data from the GISAID EpiCov database²⁷ available until 2023-04-01. For quality control, we truncate the 3' and 5' regions of sequences and remove sequences that contain more than 5% ambiguous sites or have an incomplete collection date. We align all sequences against a reference isolate from GenBank⁸⁰ (MN908947), using MAFFT v7.490.⁸¹ Then we map sequences to Variants of Concern/Interest (VOCs/VOLs), using the set of identifier amino acid changes given in Outbreak.info.²⁸ As a cross-check, we independently infer a maximum-likelihood (ML) strain tree from quality-controlled sequences under the nucleotide substitution model GTR+G of IQTree,⁸² using the reference isolate hCoV-19/Wuhan/Hu-1/2019 (GISAID-Accession: EPI ISL 402125) as root. For assessment of the tree topology, we use the ultrafast bootstrap function⁸³ with 1000 replicates. Internal nodes are timed by TreeTime⁹² with a fixed clock rate of 8×10^{-4} under a skyline coalescent tree prior.⁹³ Consistently, variants are mapped to unique genetic clades (subtrees) of the ML tree (**Figures 1C** and **4A**).

Frequency trajectories of variants

For a given variant i , we define the smoothed count $n_i(t) = \sum_{v \in I} \exp[-(t - t_v)^4 / \delta^4]$, where the sum runs over all sequences v mapped to variant i and t_v is the collection date of sequence v . We use a smoothing period $\delta = 33$ d, which gives significant weight to sequences collected at times $t \pm 15$ d. The empirical variant frequency is then defined by normalisation over all co-existing variants, $\hat{x}_i(t) = n_i(t) / \sum_j n_j(t)$. Frequencies are computed until the cutoff 2023-03-01, one month before data download. These frequency trajectories, evaluated separately for each region of this study, as well as averaged over regions, are shown in **Figure 1B**.

Infection and vaccination trajectories

Daily infection and vaccination rates for individual regions have been obtained from Ourworldindata.org²⁵ and from CDC COVID Data Tracker²⁶ for US states (download date: 2023-04-01). The resulting cumulative population fractions of infected individuals, together with cumulative population fractions of primary, booster, and bivalent booster vaccinations are reported in **Figure 1A**. Clade-specific infection rates $\omega_k(t)$ are computed by multiplying the total daily infection rates reported in each region with the simultaneous viral clade frequencies $\hat{x}_k(t)$.

Data integration for regional analysis

This study uses sequence data and epidemiological data from multiple regions for parallel analysis. Sequence data serves to infer empirical fitness trajectories for individual clades from their frequency trajectories. Epidemiological records provide input to the antigenic fitness model, **Equations 1** and **2**. The evaluation of the fitness model, which is detailed below, integrates data of both categories and requires stringent criteria of data availability and comparability between regions.

In each region, we require the following criteria for a given clade shift: (i) The smoothed sequence count $n_i(t)$ exceeds 500 sequences per day in the period from 2021 to 04-01 to 2022-09-01, which covers the majority clades from Alpha to BA.4/5. This criterion ensures that the empirical relative fitness, especially for minority frequencies, can be estimated with reasonable statistical errors. Most exclusions of regions based on insufficient sequence data. (ii) Both the invading and ancestral variant are majority variants in different time intervals for each of the major global clade shifts. This criterion excludes regions where other variants are predominant during the clade shifts (e.g., Brazil and South Africa had $\hat{x}_{\text{Alpha}} < 0.5$ throughout the 1-Alpha shift). (iv) The empirical selection trajectory \hat{s} contains at least 6 measured points $\hat{s}(t_i)$ for the Alpha-Delta clade shift, and at least 4 measured points for later clade shifts. This criterion ensures a sufficient signal-to-noise ratio for inference of temporal variation along the trajectory. (v) The total

number of reported infections exceeds 5% of the population on 2022-02-01. This criterion excludes regions with very low number of reported infections at the height of the pandemic (e.g., Japan) and ensures that cross-immunity trajectories, as given by [Equation 1](#), can be evaluated across regions with sufficient consistency. (vi) Vaccinations have been predominantly by mRNA vaccines and epidemiological records in the database are complete. This criterion ensures population immunity computed in the vaccination immune classes are comparable between regions. It excludes regions with substantial use of viral vector vaccines (e.g., the UK).

We identify a set of 13 regions that satisfy the above criteria in all clade shifts up to BA.4/5: Belgium, California (representative of US West Coast), Canada, Finland, France, Germany, Italy, Netherlands, Norway, New York (representative of US East Coast), Spain, Switzerland, US (remainder). This set is used for the longitudinal-tracking analysis of the main text (including [Figures 1, 2, 3, 4, 5, and S1](#)). The inference of model parameters and shift-specific regional analysis ([Figures S2 and S3, Data S1](#)) is performed in all regions that fulfill these criteria for a given clade shift.

Inference of empirical fitness

Using the reverse of [Equation 3](#), we infer relative fitness trajectories from regional frequency trajectories,

$$\hat{f}_i(t) = \frac{d}{dt} \log \hat{x}_i(t) \quad (\text{Equation 7})$$

with a time step $\Delta t = 30$ days for evaluation of the derivative. A hat distinguishes empirical relative fitness and frequency trajectories from their model-based counterparts introduced below. For a given variant, we compute empirical fitness trajectories, $\hat{\mathbf{f}} = (\hat{f}(t_1), \hat{f}(t_2), \dots, \hat{f}(t_n))$, for the maximal time interval such that $\hat{x}_i(t) > 0.01$ along the entire trajectory. The start point t_1 is the first day when $\hat{x}_i(t) > 0.01$. From this point, the relative fitness is recorded weekly. Single measurements $\hat{f}(t_i)$ are excluded when the sequence counts $n_i(t_i)$ is < 10 . Statistical errors for relative fitness trajectories are evaluated by binomial sampling of counts with pseudocounts of 1. In [Figure 3](#), we show trajectories of $\hat{f}_i(t)$ averaged over all longitudinally tracked regions; the corresponding regional trajectories are reported in [Figure S1](#).

The selection coefficient between the invading and ancestral variant in a clade shift equals their difference in their relative fitness, $s(t) = f_{\text{inv}}(t) - f_{\text{anc}}(t)$. From [Equation 7](#), the empirical selection coefficient between these variants takes the form

$$\hat{s}(t) = \frac{d}{dt} \log \left(\frac{\hat{x}_{\text{inv}}(t)}{\hat{x}_{\text{anc}}(t)} \right). \quad (\text{Equation 8})$$

Empirical selection trajectories for clade shifts between majority clades, $\hat{\mathbf{s}} = (\hat{s}(t_1), \hat{s}(t_2), \dots, \hat{s}(t_n))$, starting at a time t_1 when $\hat{x}_{\text{inv}}(t_1) > 0.01$ and running until a time t_n when $\hat{x}_{\text{anc}}(t_n) < 0.01$, are reported in [Data S1](#) and [Figure S2](#); these trajectories also serve the inference of antigenic model parameters detailed below.

The time dependence of empirical selection trajectories $\hat{\mathbf{s}}$ in the completed clade shifts from 1 to BQ.1 is analyzed in [Figure S2](#). We evaluate two summary statistics: (i) the amount of systematic time-dependent variation of selection, defined as $\text{Var}(s_{\text{lin}})$, averaged over regions, where $s_{\text{lin}}(t)$ is a linear regression to the ensemble of trajectories; (ii) the statistical significance of the linear regression, P (two-sided Wald test). These tests show strong and significant temporal variation the 4 clade shifts Delta–BA.1, BA.2–BA.4/5, BA.4/5–BQ.1 ($P < 10^{-11}$ and $\text{Var}(s_{\text{lin}}) > 2 \times 10^{-3}$). We find no significant time dependence for the shift 1–Alpha ($P > 0.01$) and weak time dependence ($\text{Var}(s_{\text{lin}}) = 3 \times 10^{-4}$) for BA.1–BA.2.

Cross-immunity trajectories

The antigenic, epidemic and sequence data, as described above, are combined in cross-immunity trajectories $C_i^k(t)$ that describe the total protection in a population against a given variant i , as derived from an immune class k . First, the cross-immunity factor c_i^k is defined as the relative reduction in infections by variant i induced by (recent) immunisation in class k . As shown in recent work,^{11,12} absolute titers of SARS-CoV-2 neutralisation assays can predict cross-immunity, $c_i^k = H(T_i^k)$ with

$$H(T) = \frac{1}{1 + \exp[-\lambda(T - T_{50})]}. \quad (\text{Equation 9})$$

This relation has been established in Khoury et al.¹¹ with constants $T_{50} = 4.2$ and $\lambda = 0.9$. It takes the form of a thermodynamic Hill function, consistent with the fact that functional, near-equilibrium binding of antigens and antibodies is a major determinant of neutralization. The resulting cross-immunity factors $c_i^k(\Delta t)$ include antibody decay, as given by [Equation 6](#). Hence, they depend on the time since primary immunisation,

$$c_i^k(\Delta t) = H\left(T_i^k - \frac{\Delta t}{\tau}\right). \quad (\text{Equation 10})$$

These factors enter the population cross-immunity functions $C_i^k(t)$, [Equation 1](#),

$$C_i^k(t) = \int_0^t H\left(T_i^k - \frac{t - t'}{\tau}\right) \omega_k(t') dt'. \quad (\text{Equation 11})$$

where $\omega_k(t)$ are the time-dependent population rates of immunisations in a given immune class. The cross-immunity functions inferred in this study are plotted in [Figure 2](#); they enter all evaluations of the fitness model, [Equation 2](#) ([Figures 3, 4, 5](#), and [S1](#)).

Minimal fitness model

The analysis of the main text is based on a fitness model with two main components. Intrinsic fitness depends on the clade-specific basic reproductive number, $R_{0,i}$. Antigenic fitness is mediated by population cross-immunity, which enters the epidemic dynamics through a reduction of the susceptible population and a proportional reduction of the effective reproductive number, $R_i(t)$. In a multi-strain epidemic, we describe this reduction by a multiplicative superposition of immune classes,

$$R_i(t) = R_{0,i} \exp \left[- \sum_k \gamma_k C_i^k(t) \right], \quad (\text{Equation 12})$$

This form accounts for the bookkeeping of multiple (breakthrough) infections in an individual's immune history in an approximate way⁴⁵ and has the correct asymptotics $R_i \rightarrow 0$ when $\sum_k C_i^k(t)$ becomes large. The weight factors γ_k rescale the cross-immunity functions computed from reported data to their actual fitness effect. These factors are free model parameters; their inference will be detailed below.

Linking reproductive number to epidemic growth requires a model for the distribution of time intervals between subsequent infections in a transmission chain (generation time intervals). Here we use the established form of a Gamma distribution with uniform mean τ and variance σ^2 (i.e., with shape parameter $k = \tau^2/\sigma^2$); deformations of this form will be discussed below. The clade-specific growth rate (absolute fitness) is then given by^{39,40}

$$F_i(t) = \frac{\tau}{\sigma^2} [R_i^{\sigma^2/\tau^2}(t) - 1]. \quad (\text{Equation 13})$$

For SARS-CoV-2, we use basic parameters $\tau = 5.0$ d and $\sigma^2 = 3.2$ d² obtained from averaged literature values as reported in ref. [94](#). In this parameter regime, the growth rate is well approximated by the form given in the main text,

$$F_i(t) \approx \frac{1}{\tau} \log R_i(t), \quad (\text{Equation 14})$$

as shown in [Figure S3A](#). This form becomes exact in the limit of uniform generation time intervals ($\sigma^2 \rightarrow 0$).

Combining [Equations 12](#) and [14](#), we obtain the fitness model of the main text,

$$F_i(t) = F_{0,i} - \sum_k \gamma_k C_i^k(t), \quad (\text{Equation 15})$$

where $F_{0,i} = \log R_{0,i}/\tau$ and $F_i^{ag}(t) = - \sum_k \gamma_k C_i^k(t)$ are the intrinsic and antigenic fitness components, respectively. Fitness differences (selection coefficients) between clades, $s_{ij}(t) = F_i(t) - F_j(t)$, take the form

$$s_{ij}(t) = \frac{1}{\tau} \log \frac{R_{0,i}}{R_{0,j}} - \frac{1}{\tau} \sum_k \gamma_k [C_i^k(t) - C_j^k(t)]. \quad (\text{Equation 16})$$

The minimal model has three simplifying properties. (i) Intrinsic and antigenic selection enter additively; i.e., there is no epistasis between these components. (ii) Antigenic fitness is additive in the immune classes. This is consistent with the assumption that in an infection chain, a viral lineage rapidly samples hosts randomly distributed over immune classes. (iii) Selection coefficients decouple from absolute growth, i.e., are invariant under a uniform rescaling $R_{0,i} \rightarrow aR_{0,i}$. This is important for the robustness of our inference method under non-pharmaceutical interventions, as discussed below.

Model validation

Multiple phenotypes and functions affect the viral life cycle, including the stability of viral proteins, binding to receptors of human cells, intra-cellular replication and defense against innate immunity, and transmission between hosts. All of these can be the target of intrinsic selection, by modulating the reproductive number and the distribution of generation intervals. Here we introduce three simple evolutionary deformations of the infection dynamics and analyze their consequences for the fitness model.

- (1) Changes in reproductive number. A mutation of the virus increasing its transmissibility between hosts can be assumed to increase the basic reproductive number R , while keeping the generation parameters τ and σ^2 invariant. In [Figure S3A](#), we plot the selection coefficient s of a mutant clade with increased basic reproductive number, $R_{mut} = 1.2 R_{anc}$, as a function of the antigenic selection under the minimal model, $s_{ag} = (1/\tau)[\log(R_{mut}/R_{0,mut}) - \log(R_{anc}/R_{0,anc})]$, for three values of R_{anc} (corresponding to three absolute rates of epidemic growth, F) with basic generation parameters $\tau = 5$ d and $\sigma^2 = 3.2$ d². In good approximation, selection is seen to be additive and independent of absolute growth, $s = s_0 + s_{ag}$ with $s_0 = (1/\tau)\log(R_{0,mut}/R_{0,anc})$, as given by the minimal model, [Equation 16](#).

- (2) Changes in mean generation interval. A mutation increasing the rate of intra-host replication can shorten the time to the start of transmission, while keeping the infectious period unchanged. This type of change can approximately be described by a decrease of τ at constant σ^2 and R (Figure S3B). The resulting selection coefficient remains approximately additive, $s = s_0 + s_{ag}$, but the intrinsic selection coefficient becomes dependent on absolute growth. This coupling is not described by the minimal model and, if absolute growth depends on time, introduces a time-dependence of intrinsic selection.
- (3) Correlated changes of infection parameters. Here we consider mutations that increase pathogenicity by prolonging the infectious period. This type of change can approximately be described by a correlated increase of τ , σ^2 and R , such that the time to the start of transmission remains unchanged but the end of transmission is delayed (Figure S3C). The resulting selection coefficient is additive and consistent with the minimal model, $s = s_0 + s_{ag}$, where s_0 depends on the change in the infectious period, but is approximately independent of absolute growth.

Together, mutations between variants that affect the viral replication cycle can introduce a coupling between absolute growth and selection and, in turn, generate time-dependent intrinsic selection that confounds our inference of antigenic selection as the time-dependent component of the total selection coefficient. The magnitude of this effect depends on the detailed mechanistic effects of mutations between variants, which are in general unknown. For three major variants relevant for this study, changes in the mean generation interval have been reported, from $\tau = 5.5$ d for Alpha to $\tau = 4.7$ d for Delta⁴⁹ and from $\tau = 3.8$ d for Delta to $\tau = 3.0$ d for BA.1.⁵⁰ To estimate the growth-selection coupling directly from empirical data, we record the time-dependent total growth rate and its correlation with selection for the Alpha–Delta and the Delta–BA.1 shifts (Figures S3F and S3G). We infer absolute growth trajectories,

$$\hat{F}(t) = \frac{d}{dt} \log I(t), \quad (\text{Equation 17})$$

where $I(t)$ are reported incidence values and $\hat{F}(t)$ is to be interpreted as a population mean, $\hat{F}(t) = \hat{x}_{inv}(t)\hat{F}_{inv}(t) + \hat{x}_{anc}(t)\hat{F}_{anc}(t)$ (Figure S3F). From these trajectories, we estimate the region-averaged temporal change, $\Delta\hat{F}$, over the duration of each clade shift; we find $\Delta\hat{F} = 0.07$ for Alpha–Delta and $\Delta\hat{F} = -0.02$ for Delta–BA.1. Next, we evaluate the systematic co-variation of selection and growth by means of a linear regression, $\hat{s}(t) = c\hat{F}(t) + \dots$; we find $c = 0.1$ for Alpha–Delta and $c = 0.2$ for Delta–BA.1 (Figure S3G). Hence, only a small part of the time-dependence of selection, of order $|c \Delta\hat{F}| < 0.01$, can be explained by the coupling to absolute growth induced by intrinsic selection. We conclude that antigenic changes are the dominant source of time-dependent selection, in accordance with the minimal selection model, Equation 15.

Non-pharmaceutical interventions

Such measures generate changes in social behavior that affect viral transmission, modulating the reproductive number and the distribution of generation intervals uniformly for all circulating strains. Non-pharmaceutical interventions (NPI) can have two kinds of effects:

- (1) Reduction of reproductive numbers. Mask wearing or social distancing can reduce transmission rates and generate a uniform, time dependent modulation of reproductive numbers, $R_{0,i} \rightarrow a(t)R_{0,i}$, while keeping the generation parameters τ and σ^2 invariant (Figure S3D).
- (2) Reduction of the infectious period. Surveillance and isolation measures can also reduce the effective infectious period, generating a uniform, correlated decrease of τ , σ^2 and R_0 (Figure S3E). Effects of this kind have repeatedly been reported during the SARS-CoV-2 pandemic.^{94,95}

For both kinds of interventions, we compute the selection coefficient s of an antigenic mutant clade against the corresponding selection coefficient under the minimal model, $s_{ag} = (1/\tau)[\log(R_{mut}/R_{0,mut}) - \log(R_{anc}/R_{0,anc})]$, for two values of the NPI constraint. We find that, while NPI can strongly affect absolute growth, selection coefficients are approximately independent of the NPI constraint. Hence, our selection inference is robust under time-dependent changes of NPI measures.

Inference of fitness model parameters and selection coefficients

The free parameters γ_k ($k = 1, \dots, n$) measure the fitness effect of each cross-immunity component. These parameters calibrate the model to data of real populations with complex population structure, including incidence structure and variation of infection histories, as well as heterogeneity in the monitoring of infections. To avoid overfitting, we use a minimal model with just 2 global antigenic parameters: (i) A basic rate $\gamma_{vac} = \gamma_{bst} = \gamma_{biv}$ translates cross-immunity generated by vaccination into units of selection. We infer a value γ_1 for the Alpha–Delta shift and a lower value γ_2 for all later shifts (Table S2); this value is used for all predictions. This can be seen as a heuristic to account for the effect of double infections,⁴⁸ which increase cross-immunity and decrease cross-immunity differences between variants. (ii) A uniform rate for all infection classes, $\gamma_k = b\gamma_{vac}$, includes a weight factor b accounting for underreporting of infections relative to vaccinations. We infer an initial value b_1 for all shifts up to BA.2 (inferred from data up to the completion of Delta–BA.1; the shift BA1–BA.2 involves only small antigenic effects). For the post-BA.2 period, we infer a time-dependent factor $b(t)$ from data in a sliding window [$t - 120$ d, t]. This value is used for predictions from time t into the future (Figures 4 and 5). The

selection breakdown for individual shifts ([Figures 3](#) and [S1](#), [Data S1](#); [Table S3](#)) uses posterior values inferred from data until completion of each shift: b_1 for pre-BA.2 shifts, b_2 for BA.2–BA.4/5, b_3 for BA.4/5–BQ.1 ([Table S2](#)).

The model parameters are trained on regional trajectories of selection coefficients for the majority clades. We infer the ML fitness model by aggregation of log likelihood scores evaluated for these trajectories. We use the score function

$$L(\hat{\mathbf{s}}, \mathbf{s}) = \sum_{i=1}^n \frac{(\hat{\mathbf{s}}(t_i) - \mathbf{s}(t_i))^2}{\sigma^2(t_i)}, \quad (\text{Equation 18})$$

for a single empirical selection trajectory $\hat{\mathbf{s}}$ and its model-based counterpart \mathbf{s} . The expected square deviation is $\sigma^2(t_i) = \sigma_s^2(t_i) + \sigma_0^2$; the first term describes the sampling error of sequence counts, which enters frequency and empirical selection estimates, the second term summarises fluctuations unrelated to sequence counts. The total log likelihood score is the sum $L = \sum L(\mathbf{s}, \hat{\mathbf{s}})$, which runs over all shifts in a given time interval and all included regions. We evaluate the ML score L and the corresponding BIC score⁹⁶ relative to a null model of time-independent selection ([Table S2](#)). The 95% confidence intervals of the inferred parameters are computed by resampling the empirical selection data with fluctuations σ^2 . We infer a decrease in the ML vaccination parameter ($\gamma_2 = a\gamma_1$ with $a < 1$), which is consistent with the interpretation of the parameter a as weighting factor accounting for double-infections. Similarly, we infer an ML infection weight parameter $b > 1$; the function $b(t)$ gradually increases in 2022, interpolating between the end-of-shift values $b_1 < b_2 < b_3$. This pattern is consistent with b accounting for underreporting (see above). The ML selection components resulting from our inference are reported in [Figure 3B](#) and [Table S3](#).

The inference procedure works as follows: (i) For the pre-BA.2 clade shifts, which are characterised by strong data heterogeneity between regions, we decompose model-based and empirical selection trajectories into temporal mean and change, $s(t) = \langle s \rangle + \Delta s(t)$ and $\hat{s}(t) = \langle \hat{s} \rangle + \Delta \hat{s}(t)$, where brackets denote time averages over the trajectory for a given region. In a first step, we infer the ML antigenic parameters γ_{vac} and b from the within-region selection changes $\Delta s(t)$, using the partial score $L(\Delta \hat{s}, \Delta s)$. Importantly, this inference step yields the ML antigenic model parameters and the resulting ML antigenic selection components, $s_{\text{ag}}(t) = \sum_k s_k(t)$, independently of intrinsic selection. In a second step, we infer the intrinsic selection for each shift as the difference between empirical selection and ML antigenic selection, $s_0 = \langle \langle \hat{s} - s_{\text{ag}} \rangle \rangle$, where the double brackets denote averaging over time and regions. (ii) For the post-BA.2 clade shifts, where frequency tracking data are less heterogeneous between regions, we can use a single-step inference procedure with the score function (S18). On the other hand, reported incidence numbers become highly heterogeneous in this period. Therefore, we average the population immunity functions $C_i^k(t)$ for infection-derived immune classes k_{inf} over the included regions. The post-BA.2 data turn out to be well described by an ML antigenic fitness model ($s_0 = 0$). This is important for predictions: computing the initial fitness of an emerging variant involves tracking data only of previous variants ([Figures 4B](#) and [5F](#)). Predictive analysis in this period uses a weight factor $b(t)$ inferred from data in the time window $[t - 120d, t]$ with daily updates from $t = 2022-05-09$ (start of the clade shift BA.2–BA.4/5); window segments before this date are weighed in proportionally with the initial value b_1 .

Significance analysis of the fitness model

To assess the statistical significance of our inference, we compare four fitness models of the form of [Equation 2](#): the full model used in the main text (VAC+INF: antigenic selection by vaccination and infection, intrinsic selection), two partial models (VAC: antigenic selection only by vaccination, intrinsic selection; INF: antigenic selection only by infection, intrinsic selection), and a null model (0: intrinsic selection only). We infer conditional ML parameters for each model and we rank models by their ML score difference to the null model, $\Delta L = L - L_0$ ([Table S2](#)). An alternative ranking by BIC score,⁹⁶ which contains a score penalty for the number of model parameters, leads to the same result. Both scores are reported separately for the pre-BA.1 period and for the full inference period.

We obtain the following results: (i) The antigenic fitness models VAC+INF and INF have significantly higher scores than the null model, which shows that the empirical selection data are incompatible with time-independent selection. (ii) The full model has a significantly higher score than any of the other models. Hence, both vaccination and infection are significant components of antigenic selection. (iii) The partial antigenic model VAC has a higher score than INF for the pre-BA.1 shifts, but a lower score than the null model in the post-BA.2 period. Hence, vaccinations explain a substantial part of the pre-BA.1 pattern, but vaccinations alone do not capture the later data.

In summary, we infer a statistically significant fitness model with few, global parameters from sequence and epidemiological data aggregated over a set of regions and combined with antigenic data. The model describes common time-dependent patterns of selection in these regions and serves three main purposes: to provide a breakdown of selection in intrinsic and antigenic components ([Figure 3](#)), to infer ML antigenic parameters used in the prediction of short-term frequency turnover ([Figure 4](#)), and to compute antigenic profiles for emerging variants ([Figure 5](#)). Our inference procedure rests on stringent criteria for the joint availability of sequence and epidemiological data in each of these regions (as listed above). The results are robust under variation of the inclusion criteria for regions. In particular, the signal of antigenic selection in data and model is broadly distributed over regions ([Data S1](#)). Hence, the selection averages reported in [Figure 3](#) and [Table S3](#) are reproducible in subsampled sets of regions.

Prediction of frequency trajectories

In the post-BA.2 evolutionary regime, we predict short-term relative frequency changes, $W_i(t, t + \tau) = x_i(t + \tau)/\hat{x}_i(t)$, with a prediction period $\tau = 60$ d, for the variants BA.2, BA.4/5, BA.4.6, BF.7, BQ.1, BN.1, XBB, CH.1. By integrating [Equation 3](#) to leading order in the prediction period, we write

$$W_i(t, t') = \frac{1}{Z(t, t')} \exp [-(t' - t) f_i(t)], \quad (\text{Equation 19})$$

where $f_i(t)$ is evaluated at the start of prediction and $Z(t, t')$ is a normalisation factor ($0 \leq t' \leq t + \tau$). Here we use only the antigenic fitness, $f_i^{\text{ag}}(t)$, as given by Equations 1 and 2. Short-term predictions are shown in Figure 4B for all longitudinally tracked regions and up to 6 starting points on each regional trajectory, together with the posterior changes $\widehat{W}_i(t, t + \tau) = \widehat{x}_i(t + \tau)/\widehat{x}_i(t)$ obtained by tracking of frequency trajectories.

Longer-term predictions of frequency changes serve to flag likely shifts of majority clades driven by emerging variants. These predictions start when a new variant has reached a global frequency $\widehat{x}(t) = 0.01$ and extend over a prediction period of $\tau = 200$ d, using again Equation 19. The resulting trajectories $y_i(t') = W(t, t') \widehat{x}_i(t)$ ($0 \leq t' \leq t + \tau$) are to be interpreted as reduced frequencies in the set of variants present at the start of predictions, ignoring variants that emerge later. Predicted and posterior region-averaged trajectories are shown in Figure 4C. A likely predominance shift is flagged if an emerging variant reaches a predicted frequency $y(t') > 0.5$ within the prediction period (thick lines in Figure 4C).

The prediction procedure has the following specifics: (i) We use tracking data up to the start of predictions. Smoothened empirical frequencies $\widehat{x}_i(t)$ include submitted sequences in the period $[t - 15, t + 15]$ days. Therefore, we choose an integration period $\tau' = \tau + 15$ d to obtain a genuine prediction over a period τ into the future. (ii) We use fitness model parameters inferred prior to the start of predictions, as detailed above (specifically, infection parameters $b(t - 15\text{d})$). (iii) The population immunity functions, $C_i^k(t)$, for infection-derived immune classes are averaged over regions, taking into account the heterogeneity of tracking across regions in the prediction period. (iv) We include predictions for all variants that reach 5% regional frequency after 2022-04-01 in at least 1 of 13 longitudinally tracked regions. Predictions of this study end at a cutoff date 2023-03-01 (one month before the download date of data). (v) For short-term predictions, up to 6 starting points are chosen on each regional trajectory at the following frequencies: $\widehat{x}_i = 0.01, 0.2, 0.4$ (ascending segment), $\widehat{x}_i/\widehat{x}_{i,\text{max}} = 1, 0.5, 0.25$ (descending segment). (vi) Longer-term predictions start when a new variant reaches a region-averaged frequency threshold $\widehat{x}_i(t) = 0.01$. If further variants emerge at the same threshold within 14 days, the prediction windows are merged. In this way, we obtain 4 prediction windows starting on 2022-07-12 (emerging variants BA.4.6 and BF.7), 2022-09-06 (emerging variant BQ.1), 2022-10-22, (emerging variants BM.1.1, BN.1, and XBB), and 2022-12-08 (emerging variant CH.1). (vii) Statistical errors are calculated by resampling the number of observed sequences of each of the competing variants. This reflects the uncertainty of the empirical frequency trajectories, $\widehat{x}_i(t)$, which set the uncertainty in the initial condition for predictions. The error bars in Figure 4B indicate one standard deviation.

Antigenic selection profiles

To predict the likely direction of antigenic evolution, we compute the antigenic selection profile, $s_{\text{ag}}(t) = \sum_k s_k(t)$, for a hypothetical “standard” mutant emerging at time t and competing against the majority background variant present at that time (Figure 5). We use again the fitness model, $s_{\text{ag}}(t) = \sum_k \gamma_k [C_{\text{mut}}^k(t) - C_{\text{anc}}^k(t)]$ with cross-immunity functions given by Equation 1. In the computation of cross-immunity, we assume the mutant has an antigenic advance, or neutralisation titer drop, $T_{\text{anc}}^k - T_{\text{mut}}^k = 2$ in all relevant immune classes k . These assumptions are supported by observations. The circulating viral population has sufficient supply of mutations for timely response to antigenic selection pressures, which justifies the assumption of a broad response across immune classes (Figure 5F). The amplitudes of antigenic advance assumed for the standard mutant are similar to the observed values of successful mutants (Figures 5A–5E). The computation of the antigenic selection profile $s_{\text{ag}}(t)$ uses model parameters inferred up to time t (as detailed above), as well as epidemiological, frequency tracking, and antigenic data up to time t . Importantly, the computation does not depend on antigenic data of the emerging mutant itself. Hence, the antigenic selection profiles can be evaluated prior to the emergence of an actual escape mutant. These profiles predict likely antigenic characteristics of high-fitness antigenic variants conditional on their emergence time (Figure 5F).

For the observed escape mutants, we can compare antigenic and fitness effects obtained from our analysis with deep mutational scanning (DMS) data. For example, Cao et al.¹⁰ performed DMS of recent SARS-CoV-2 variants different in immune backgrounds and obtained normalised, weighted escape scores for individual point mutations in the receptor binding domain (RBD). For the RBD mutations that distinguish the variants BA.4.6, BF.7, BQ.1, and XBB from their recent ancestor BA.4/5, we list the normalised, averaged DMS escape scores against BA.4/5 breakthrough infections (data from Cao et al.¹⁰).

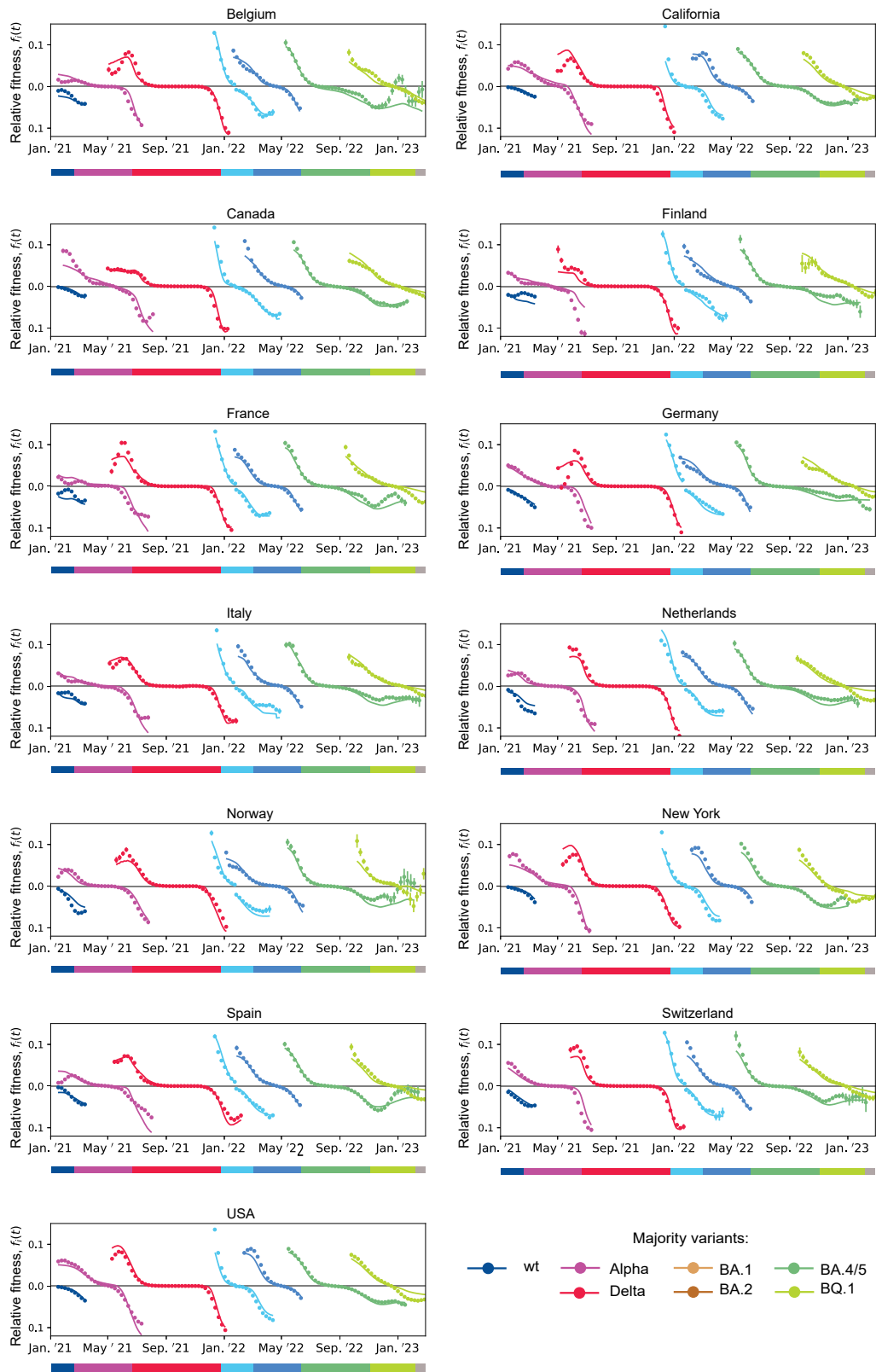
	346T	368I	444T	445P	446S	452R	460K	490S	Total score
BA.4.6	0.30	-	-	-	-	0.0	-	-	0.30
BF.7	0.30	-	-	-	-	0.0	-	-	0.30
BQ.1	0.30	-	1.0	-	-	0.0	0.04	-	1.34
XBB	0.30	0.0	-	0.29	0.30	-	0.04	0.01	0.94

Each of these variants has between 2 and 6 point mutations in the listed set of RBD positions. We compute the resulting total score as the sum of the scores of individual mutations, which ranks these variants in their escape potential from immunity induced by BA.4/5 breakthrough infections. The variants BA.4.6, BF.7, BQ.1 compete on the antigenic background of the major variant BA.4/5, the variant XBB competes later against the major variant BQ.1 (main text, [Figure 5F](#)). The DMS score ranking is in accordance with the large antigenic advance of BQ.1 in immune class $k = \text{BA.4/5}$ ([Figure 5C](#)) and the resulting fitness advantage against BA.4.6 and BF.7, as found in our analysis ([Figure 4C](#)). This example shows how DMS data can serve as input for antigenic selection profiles and fitness predictions. However, the score ranking does not reproduce the initial antigenic advance and the resulting fitness gain of the recombinant variant XBB against BQ.1 ([Figures 5D and 4C](#)). This may indicate epistasis between some of these mutations or reflect the admixture of other immune classes in the antigenic selection profiles ([Figure 5F](#)).

QUANTIFICATION AND STATISTICAL ANALYSIS

Statistical analyses were performed using Scipy version 1.10.1 and are described in the figure legends and in the [method details](#).

Supplemental figures



(legend on next page)

Figure S1. Regional fitness trajectories, related to Figure 3

Relative fitness of successive major variants in 7 completed clade shifts (1–Alpha, ..., BA.4/5–BQ.1) for all longitudinally tracked regions of this study. Model-based trajectories for each variant, $f_i(t)$ (lines), are shown for the duration of each clade shift; empirical fitness values, $\hat{f}_i(t)$ (dots), are inferred from regional frequency trajectories (Figure 1B). Color bars mark the succession of major variants. Vertical error bars indicate one standard variation. Criteria for inclusion of regions are given in STAR Methods; see Figure 2 for region-averaged trajectories.

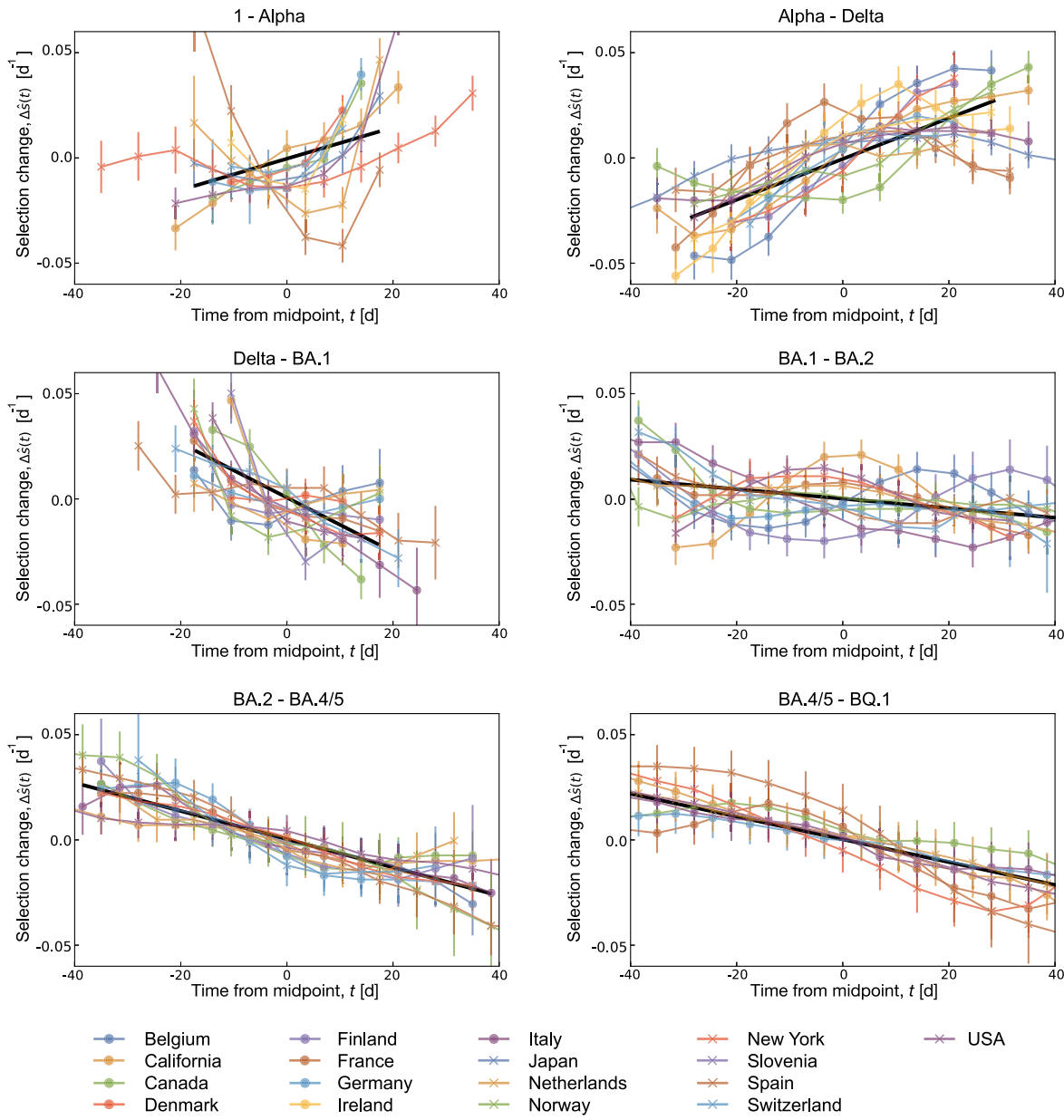


Figure S2. Time dependence of selection, related to Figure 3

Empirical selection change between invading and ancestral clade, $\Delta\hat{s}(t) = \hat{s}(t) - \langle s \rangle$, for all completed clade shifts and all longitudinally tracked regions of this study (brackets denote time averages for each trajectory). Selection trajectories are derived from regional frequency trajectories and plotted against time counted from the midpoint (colored lines); vertical error bars indicate the 95% confidence interval. Summary statistics: cross-region linear regression, $s_{lin}(t)$ (black solid line, length gives r.m.s. time span of trajectories).

- (A) 1-Alpha: small, statistically insignificant time dependence, $\text{Var}(s_{lin}) = 6.5 \times 10^{-4}$, $p > 0.01$.
- (B) Alpha-Delta: substantial, statistically significant time dependence, $\text{Var}(s_{lin}) = 3.0 \times 10^{-3} d^{-2}$, $p < 10^{-13}$.
- (C) Delta-BA.1: substantial, statistically significant time dependence, $\text{Var}(s_{lin}) = 1.9 \times 10^{-3} d^{-2}$, $p < 10^{-11}$.
- (D) BA.1-BA.2: small but statistically significant time dependence, $\text{Var}(s_{lin}) = 3.3 \times 10^{-4} d^{-2}$, $p < 10^{-3}$.
- (E) BA.2-BA.4/5: substantial, statistically significant time dependence, $\text{Var}(s_{lin}) = 2.6 \times 10^{-3} d^{-2}$, $p < 10^{-50}$.
- (F) BA.4/5-BQ.1: substantial, statistically significant time dependence, $\text{Var}(s_{lin}) = 5.5 \times 10^{-3} d^{-2}$, $p < 10^{-50}$.

All p values are computed using a two-sided Wald test. The statistical grading of shifts is described and criteria for inclusion of regions are given in [STAR Methods](#).

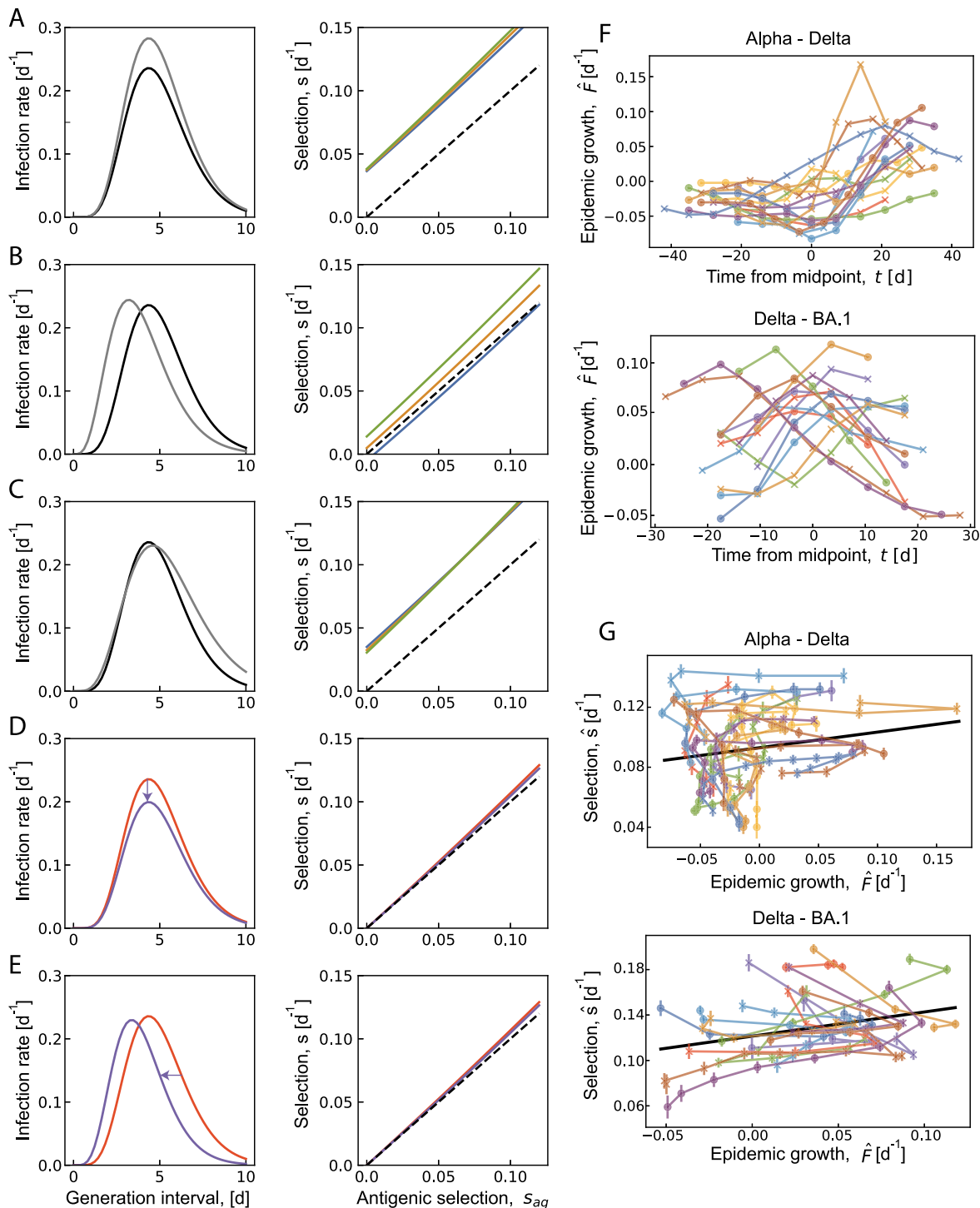


Figure S3. Selective effects of infection dynamics, related to Figure 2

(A–C) Evolution of the infection cycle. Left: Infection rate as a function of the time since the previous infection (generation interval) for two competing variants (ancestral, black; mutant, gray). This function has three parameters: reproductive number (area under the curve), R ; mean and variance of generation intervals, τ and σ^2 . Right: Total selection coefficient between invading and ancestral variants, s (colored lines), plotted against the antigenic selection component, s_{ag} , for 3 values of the ancestral growth rate (given by $R_{anc} = 0.9, 1.1, 1.3$). Selection is computed from the full fitness model, [Equation 13](#); the difference between s and s_{ag} (dashed identity line) is the intrinsic selection, s_0 . Evolutionary changes in the mutant: (A) increase in reproductive number, R ; (B) decrease in mean generation time interval, τ ; (C) correlated increase of infection parameters R, τ, σ^2 ([STAR Methods](#)).

(legend continued on next page)

(D and E) Non-pharmaceutical interventions (NPI). Left: temporal or regional changes of NPI affecting the infection dynamics uniformly for all circulating variants. Right: Total selection coefficient between invading and ancestral variants, s , plotted against the antigenic selection component, s_{ag} . Types of intervention effects: (D) reduction of reproductive numbers, R ; (E) reduction of the infectious period, correlated decrease of R , τ , σ^2 ([STAR Methods](#)).
(F) Time change of the observed epidemic growth, \hat{F} , during the Alpha–Delta and Delta–BA.1 clade shifts in all regions included in this study (see [Figure S1](#)).
(G) Empirical selection, $\hat{s}(t)$, plotted against observed epidemic growth, $\hat{F}(t)$, for the Alpha–Delta and Delta–BA.1 clade shifts (colored lines). Linear regression, $\hat{s}_{lin} = c\hat{F}$ (black line).